AD-A138 145 DEVELOPMENT OF A COMPLETE MODEL OF TURBULENCE REVISITED 1/1
(U) DCW INDUSTRIES INC LA CANADA CA D C WILCOX DEC 83
DCW-R-29-01 ARO-19572.1-EG-S DAAG29-83-C-0003

UNCLASSIFIED F/G 20/4 NL

END
DATE
FILMED
3-84
DTIC

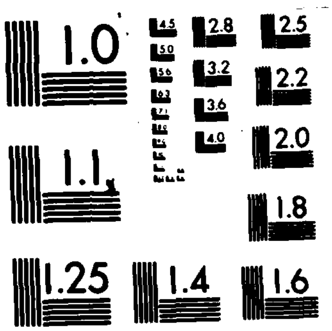

MICROCOPY RESOLUTION TEST CHART
NATIONAL BUREAU OF STANDARDS-1963-A

②

ARO 19572.1-EG

DCW-R-29-01

ADA138145

DEVELOPMENT OF A COMPLETE MODEL OF TURBULENCE REVISITED

by

David C. Wilcox

December 1983

DTIC
ELECTE
FEB 16 1984
S A

Prepared for

U.S. ARMY RESEARCH ORGANIZATION
Research Triangle Park, North Carolina

Under Contract DAAG-29-83-0003

DCW INDUSTRIES, INC.
5354 Palm Drive
La Canada, California 91604
213/790-3844

Unclassified

SECURITY CLASSIFICATION OF THIS PAGE *(When Data Entered)*

REPORT DOCUMENTATION PAGE

READ INSTRUCTIONS BEFORE COMPLETING FORM

1. REPORT NUMBER 19572.1-EG-S	2. GOVT ACCESSION NO. AD-A138 145	3. RECIPIENT'S CATALOG NUMBER
4. TITLE *(and Subtitle)* Development of a Complete Model of Turbulence Revisited		5. TYPE OF REPORT & PERIOD COVERED Technical Report
		6. PERFORMING ORG. REPORT NUMBER
7. AUTHOR(s) David C. Wilcox		8. CONTRACT OR GRANT NUMBER(s) DAAG-29-83-C-0003
9. PERFORMING ORGANIZATION NAME AND ADDRESS DCW Industries, Inc. 5354 Palm Drive La Canada, California 91604		10. PROGRAM ELEMENT, PROJECT, TASK AREA & WORK UNIT NUMBERS N/A
11. CONTROLLING OFFICE NAME AND ADDRESS U. S. Army Research Office Post Office Box 12211 Research Triangle Park, NC 27709		12. REPORT DATE Dec 1983
		13. NUMBER OF PAGES 55
14. MONITORING AGENCY NAME & ADDRESS *(if different from Controlling Office)*		15. SECURITY CLASS. *(of this report)* Unclassified
		15a. DECLASSIFICATION/DOWNGRADING SCHEDULE

16. DISTRIBUTION STATEMENT *(of this Report)*

Approved for public release; distribution unlimited.

17. DISTRIBUTION STATEMENT *(of the abstract entered in Block 20, if different from Report)*

18. SUPPLEMENTARY NOTES

The view, opinions, and/or findings contained in this report are those of the author(s) and should not be construed as an official Department of the Army position, policy, or decision, unless so designated by other documentation

19. KEY WORDS *(Continue on reverse side if necessary and identify by block number)*

Turbulence Models
Perturbation Methods
Boundary Layers
Pressure Gradients
Equations of Motion
Defect-Layer Analysis

20. ABSTRACT *(Continue on reverse side if necessary and identify by block number)*

A comprehensive and critical review of closure approximations for two-equation turbulence models has been made. Particular attention has focused upon the scale-determining equation in an attempt to find the optimum choice of dependent variable and closure approximations. Using a combination of singular perturbation methods and numerical computations, this report demonstrates: (a) conventional $k-\epsilon$ and $k-\omega^2$

20. ABSTRACT CONTINUED

formulations generally are inaccurate for boundary layers in adverse pressure gradient; (b) using so-called "wall functions" tends to mask such models' shortcomings; and (c) there exists a more suitable choice of dependent variables which is far more accurate for adverse pressure gradient.

ABSTRACT

A comprehensive and critical review of closure approximations for two-equation turbulence models has been made. Particular attention has focused upon the scale-determining equation in an attempt to find the optimum choice of dependent variable and closure approximations. Using a combination of singular perturbation methods and numerical computations, this report demonstrates: (a) conventional $k-\varepsilon$ and $k-\omega^2$ formulations generally are inaccurate for boundary layers in adverse pressure gradient; (b) using so-called "wall functions" tends to mask such models' shortcomings; and (c) there exists a more suitable choice of dependent variables which is far more accurate for adverse pressure gradient.

A-1

CONTENTS

1. INTRODUCTION

During the past fifteen years, a great deal of research has focused upon the task of devising closure approximations for the long-time-averaged Navier-Stokes equations suitable for predicting properties of turbulent flows. Prior to 1968, virtually all turbulence closure schemes were "incomplete", i.e., their implementation required some advance knowledge about the flowfield under consideration in order to obtain a solution. The best known incomplete turbulence model is the mixing-length model (Ref 1). This model is incomplete as the appropriate form of the mixing length must be determined empirically for each new application; in general, it cannot be specified a priori.

In 1968, the first "Stanford Olympiad" (Ref 2) was held to test existing turbulence models against the best experimental data available. The data base was confined to incompressible two-dimensional boundary layers. Interestingly, the competition was more-or-less won by the "complete" model of Bradshaw, et al (Ref 3).

Perhaps spurred on by the success of the Bradshaw model, the trend in turbulence modeling since the first Stanford Olympiad has been toward development of complete models. For clarity, note that the terminology "complete model of turbulence" as used in this report means a set of equations which can be used to predict a given turbulent flow with no advance information other than boundary conditions required in order to achieve a solution. The terminology is not intended to imply anything with regard to the range of applicability of the theory.

Over the past decade, the most vigorous modeling efforts have been conducted by Donaldson, et al (Ref 4), Launder, et al (Ref 5), and Wilcox, et al (Refs 6-9). Recognizing the substantial progress the various researchers seemed to be making, the second "Stanford Olympiad" was held in 1980 and 1981 (Ref 10). This time, however, the scope of the experimental data was expanded tremendously to include complicating effects of compressibility, streamline curvature, surface mass transfer, boundary-layer separation, secondary motions, etc. That is, virtually every complicating effect known to man was included in the Olympiad if experimental data of reliable quality existed.

From this researcher's viewpoint, the results of the Second of the two Stanford Olympiads were at once very encouraging and dissapointing. On the one hand, the state of the art has been shown to have advanced far beyond the wildest dreams of evaluators of the First Olympiad. It was hard to imagine in 1968 that separated flowfields could be routinely predicted with any degree of accuracy just fifteen short years later. [Of course, turbulence modelers should receive only part of the credit; magnificent advances in numerical methods such as those of MacCormack (Ref 11) have played a very important role to say the least!] On the other hand, while such predictions can be routinely made, obtaining results consistent with experimental measurements is not nearly as routine. Far worse, it is not even clear from the results presented at Stanford Olympiad 2 that we can predict effects of an adverse pressure gradient on the turbulent boundary layer any more accurately than we could fifteen years ago. Clearly, our progress in turbulence modeling has been a bit uneven.

In light of this situation, this study has been initiated with the objective of first taking a modest step backward by reviewing and assessing the original closure approximations for the class of turbulence models known as two-equation models, viz, closure being accomplished using the long-time-averaged Navier-Stokes equations and two additional differential equations. The rationale for starting at what would seem to be a very elementary level stems from a key observation made at the Second Olympiad, viz, the greatest amount of uncertainty and controversy over two-equation and higher-order models lies in the scale-determining equation. It is even unclear as to what the optimum choice of dependent variables is for a two-equation model. As a result of this study, we feel we have found the optimum choice and, based upon this choice, we have postulated a new two-equation turbulence model.

Section 2 summarizes the new model, including arguments which set values of all but two of the closure coefficients appearing in the postulated equations. Section 3 presents results of a perturbation analysis of the incompressible defect layer, including effects of pressure gradient. Predictions of the new model are compared with those of the Jones-Launder (Ref 5) and the Wilcox-Rubesin (Ref 9) models. Section 4 uses perturbation methods to analyze the viscous sublayer, including effects of surface roughness and surface mass injection. Section 5 presents results of application of the model to five incompressible boundary layers. The concluding section includes a summary of results obtained in this study.

2. EQUATIONS OF MOTION

In this section, we state the postulated equations of motion, including established values of all closure coefficients. Physical interpretations of turbulence field properties are given and, additionally, arguments are presented which have been used in setting values of several of the closure coefficients.

2.1 POSTULATED EQUATIONS

For general incompressible turbulent fluid flows, the turbulence model equations are as follows.

Mass Conservation

$$\frac{\partial u_i}{\partial x_i} = 0 \tag{1}$$

Momentum Conservation

$$\frac{\partial u_i}{\partial t} + u_j \frac{\partial u_i}{\partial x_j} = -\frac{1}{\rho}\frac{\partial p}{\partial x_i} + \frac{\partial \tau_{ji}}{\partial x_j} \tag{2}$$

Turbulent Mixing Energy

$$\frac{\partial k}{\partial t} + u_j \frac{\partial k}{\partial x_j} = \tau_{ij}\frac{\partial u_i}{\partial x_j} - \beta^* k\omega + \frac{\partial}{\partial x_j}\left[(\nu+\sigma^*\nu_T)\frac{\partial k}{\partial x_j}\right] \tag{3}$$

Turbulent Dissipation Rate

$$\frac{\partial \omega}{\partial t} + u_j \frac{\partial \omega}{\partial x_j} = \gamma S_{ij} S_{ji} - \beta\omega^2 + \frac{\partial}{\partial x_j}\left[(\nu+\sigma\nu_T)\frac{\partial \omega}{\partial x_j}\right] \tag{4}$$

where t is time and x_i is the position vector; u_i denotes long-time averaged velocity vector; p, ρ, and ν are mean pressure, density, and kinematic viscosity; and τ_{ij} is the Reynolds-stress tensor. The turbulent mixing energy, k, and the turbulent dissipation rate, ω, are needed to define the eddy diffusivity, ν_T, which is given by

$$\nu_T = \gamma^* k / \omega \tag{5}$$

The Reynolds-stress tensor is assumed proportional to the mean strain rate tensor, S_{ij}, so that we write

$$\tau_{ij} = 2\nu_T S_{ij} - \frac{2}{3} k \delta_{ij} \tag{6}$$

where, by definition,

$$S_{ij} = \frac{1}{2}\left[\frac{\partial u_i}{\partial x_j} + \frac{\partial u_j}{\partial x_i}\right] \tag{7}$$

Several closure coefficients, viz, β, β^*, γ, γ^*, σ, and σ^* appear in Equations (3-5). A key objective of this study has been to review typical arguments used in establishing values of such coefficients in a model of this type. In the next subsection and in later sections, the arguments are presented. For convenience, the values are summarized in the following equations.

$$\left.\begin{array}{llll} \beta = 3/40 & , & \beta^* = 9/100 \\ \gamma = 5/9 & , & \gamma^* = 1 \\ \sigma = 1/2 & , & \sigma^* = 1/2 \end{array}\right\} \tag{8}$$

Before proceeding to further discussion of the closure coefficients, it is worthwhile to pause and discuss the form of the model equations and the physical meanings of the quantities k and ω. As in other two-equation models of turbulence, the quantity k represents a measure of the kinetic energy of the turbulence. Whether k is specifically identified as being the exact kinetic energy of the turbulence or alternatively as the kinetic energy of the fluctuations in the direction of shear (Ref 8) is not critically important. All we require on physical grounds is that k be proportional to the square of the velocity at which local turbulent mixing occurs. The second quantity introduced in the model, ω, is referred to as the turbulent dissipation rate. Its dimensions are inversely proportional to time and it is, in fact, the same variable used by this author in all prior turbulence modeling studies. Perhaps the simplest physical interpretation of ω is that it is the ratio of the turbulent dissipation, ϵ, to the turbulent mixing energy. Alternatively, ω is the rate of dissipation of turbulence per unit energy.

As is obvious from inspection of Equation (3), the equation for k is modeled directly after the exact, long-time-averaged equation for the turbulent kinetic energy. On this point, the model is consistent with virtually all other two-equation models. The second of the two model equations is similar in form to the equation for k. Although it adds no rigor to the approach, the equation for ω can be regarded as the modeled form of the equation which would result from (a) writing the exact equations for turbulent kinetic energy and dissipation and, (b) making the formal change of dependent variables defined by

$$\omega = \varepsilon/(\beta^* k) \tag{9}$$

The primary difference between the model postulated in this study and those of this author's prior research is the form of the equation for ω. Most notably, past studies have written the equation in terms of the square of ω. Interestingly, the first two-equation model in which the variables k and ω were used was postulated by Kolmogorov (Ref 12) and his equation for ω was written in terms of ω rather than ω^2. The reason for this choice will become quite clear in Section 3 where we analyze model-predicted structure of the defect layer.

2.2 ESTABLISHING CLOSURE COEFFICIENT VALUES

In this subsection, we present straightforward arguments from which values of the four closure coefficients, β, β^*, γ, and γ^* can be established. A review of the arguments generally presented indicates the following are as physically sound as possible within the context of two-equation turbulence models.

Considering first the coefficient γ^*, we can rewrite Equations (3-6) in terms of the quantity ω/γ^*. Inspection of the resulting equations shows that this rescaling of ω is equivalent to setting $\gamma^* = 1$. Hence, with no loss of generality, we conclude that the value of γ^* is indeed unity.

Next, we turn to the ratio of β^* to β. For decaying homogeneous, isotropic turbulence, Equations (3-4) simplify to

$$\left.\begin{aligned} dk/dt &= -\ \beta^* k\omega \\ d\omega/dt &= -\ \beta\omega^2 \end{aligned}\right\} \tag{10}$$

from which the asymptotic solution for k is readily found to be

$$k \sim t^{-\beta^*/\beta} \tag{11}$$

Experimental observations indicate that $k \sim t^{-6/5}$ for decaying homogeneous, isotropic turbulence which implies $\beta^*/\beta = 6/5$ which is consistent with Equations (8).

Values for the coefficients γ and β^* can be established by examining the so-called "wall layer". The wall layer is defined as the portion of the boundary layer sufficiently distant from the surface that molecular viscosity is negligible relative to eddy viscosity, yet close enough for convective effects to be negligible relative to the rate at which the turbulence is being created and destroyed. In the limiting case of a constant-pressure boundary layer, Equations (2-7) simplify to

$$\left.\begin{aligned} 0 &= \frac{\partial}{\partial y}\left[\nu_T \frac{\partial u}{\partial y}\right] \\ 0 &= \nu_T\left[\frac{\partial u}{\partial y}\right]^2 - \beta^* k\omega + \sigma^* \frac{\partial}{\partial y}\left[\nu_T \frac{\partial k}{\partial y}\right] \\ 0 &= \gamma\left[\frac{\partial u}{\partial y}\right]^2 - \beta\,\omega^2 + \sigma\frac{\partial}{\partial y}\left[\nu_T \frac{\partial \omega}{\partial y}\right] \end{aligned}\right\} \qquad (12)$$

We seek the conditions under which these simplified equations yield a solution consistent with the law of the wall, i.e., velocity varying linearly with the logarithm of distance from the surface. As can be easily verified, Equations (12) do indeed possess a solution consistent with the law of the wall, viz,

$$\left.\begin{aligned} u &= \frac{u_\tau}{\kappa}\ell n(u_\tau y/\nu) + \text{constant} \\ k &= u_\tau^2/\sqrt{\beta^*} \\ \omega &= u_\tau/(\sqrt{\beta^*}\,\kappa\, y) \end{aligned}\right\} \qquad (13)$$

where u_τ is the conventional frictional velocity and κ is Karman's constant. There is one constraint imposed in the solution to Equations (12), namely, a unique relation exists between the implied value of Karman's constant and the various closure coefficients. Specifically, the following equation must hold.

$$\gamma = \beta/\beta^* - \sigma\kappa^2/\sqrt{\beta^*} \qquad (14)$$

Additionally, note that the Reynolds shear stress, τ, is constant in the wall layer and is equal to u_τ^2. Finally, inspection of Equations (13) shows that this implies $\tau/k = \sqrt{\beta^*}$ in the wall layer. A variety of experimental measurements (Ref 13) indicate the ratio of τ to k is about 3/10 in the wall layer. Thus, the predicted wall-layer solution is consistent with experimental observations provided $\beta^* = 9/100$.

In summary, the arguments presented in this subsection are sufficient to uniquely set the values of β, β^*, and γ^*. Also, Equation (14) determines γ in terms of the, as yet undetermined, value of σ. As a byproduct of analysis in the next section, values for the two closure coefficients σ and σ^* will be established.

3. DEFECT-LAYER ANALYSIS

In this section we use singular perturbation methods to analyze model-predicted structure of the classical defect layer. The analysis presented is a generalization of that done by Wilcox and Traci (Ref 8). In contrast to the Wilcox and Traci analysis, effects of pressure gradient have been included. Additionally, the analysis has been done for three turbulence models, viz: the model postulated in Equations (1-8); the Wilcox-Rubesin (Ref 9) model; and the Jones-Launder (Ref 5) model. First, we review details of the perturbation solution procedure. Next, we compare solutions for the three models in the absence of pressure gradient. Then, effects of pressure gradient are studied for the three models. Finally, we justify the values chosen for the closure coefficients σ and σ^* .

3.1 PERTURBATION SOLUTION

In the past, the only detailed analyses of the defect layer for any turbulence model have been those of Bush and Fendell (Ref 14 - for the mixing-length model) and Wilcox and Traci. In neither case were effects of pressure gradient delineated. In this section we extend the Wilcox-Traci analysis to include pressure gradient.

To study the defect layer, we seek a perturbation solution. The expansion proceeds in terms of the ratio of friction velocity to the boundary-layer-edge velocity, u_τ/U_e, and the dimensionless vertical coordinate, η , defined by

$$\eta = \frac{u_\tau}{U_e}\frac{y}{\delta^*} \tag{15}$$

where δ^* is displacement thickness. For the sake of brevity, we confine details of the expansion procedure to Appendix A. It is instructive to note that the velocity is given by

$$\frac{u}{U_e} = 1 - \frac{u_\tau}{U_e} U_1(\eta) + \ldots \tag{16}$$

which, to order u_τ/U_e , can be rewritten as

$$\frac{U_e - u}{u_\tau} = f(y/\Delta) \quad ; \qquad \Delta = U_e\delta^*/u_\tau \tag{17}$$

The coordinates appearing in Equation (17) are the classical defect-layer coordinates. Additionally, it is important to note that pressure gradient appears in the equations of motion in dimensionless form as

$$\beta_T = \delta^*(dp/dx)/\tau_w \tag{18}$$

where τ_w is the surface shear stress. Coles and Hirst (Ref 2) refer to β_T as the equilibrium parameter.

In order to solve the defect-layer equations, we have used an improved version of the implicit time-marching program developed by Wilcox and Traci. That is, we add unsteady terms to each of the equations of motion, make an educated guess of the solution and integrate over time until the solution displays negligible temporal variation. Computations have been done using 31, 51 and 71 points in the grid normal to the surface to determine solution sensitivity to the numerical algorithm. For all three models considered, differences between solutions obtained using 31 and 71 mesh points are less than two percent. Results of all computations given in this section have been obtained using 51 mesh points.

3.2 FLAT-PLATE BOUNDARY LAYER

Figure 1 compares numerical predictions of the three models with corresponding experimental data of Weighardt (Ref 2). (Note that in the new model computation we use $\sigma = \sigma^* = 1/2$; we defer any further discussion of the appropriate values to Subsection 3.4.) The experimental data presented are those at the highest Reynolds number for which data are reported. This is consistent with the defect-layer solution which is formally valid for very large Reynolds number. Numerical results are shown for three models, viz, the new (NEW) model, the Wilcox-Rubesin (W-R) model, and the Jones-Launder (J-L) model.

As shown, all three models predict velocity profiles which differ from measured values by no more than about three percent of scale. Interestingly, the new model shows the smallest differences from the Weighardt data. Additionally, skin friction, c_f, can be inferred from the defect-layer solution (see Appendix A). Corresponding computed and measured values are summarized in the insert on Figure 1; the largest difference is less than three percent. Thus, based on analysis of the constant-pressure defect layer, there is little difference amongst the three models.

3.3 EFFECTS OF PRESSURE GRADIENT

Turning now to the effect of pressure gradient, we have computed defect-layer solutions for the equilibrium parameter, β_T, ranging from −0.5 to +9.0. Note that positive β_T corresponds to an adverse pressure gradient. The choice of this range of β_T has been dictated

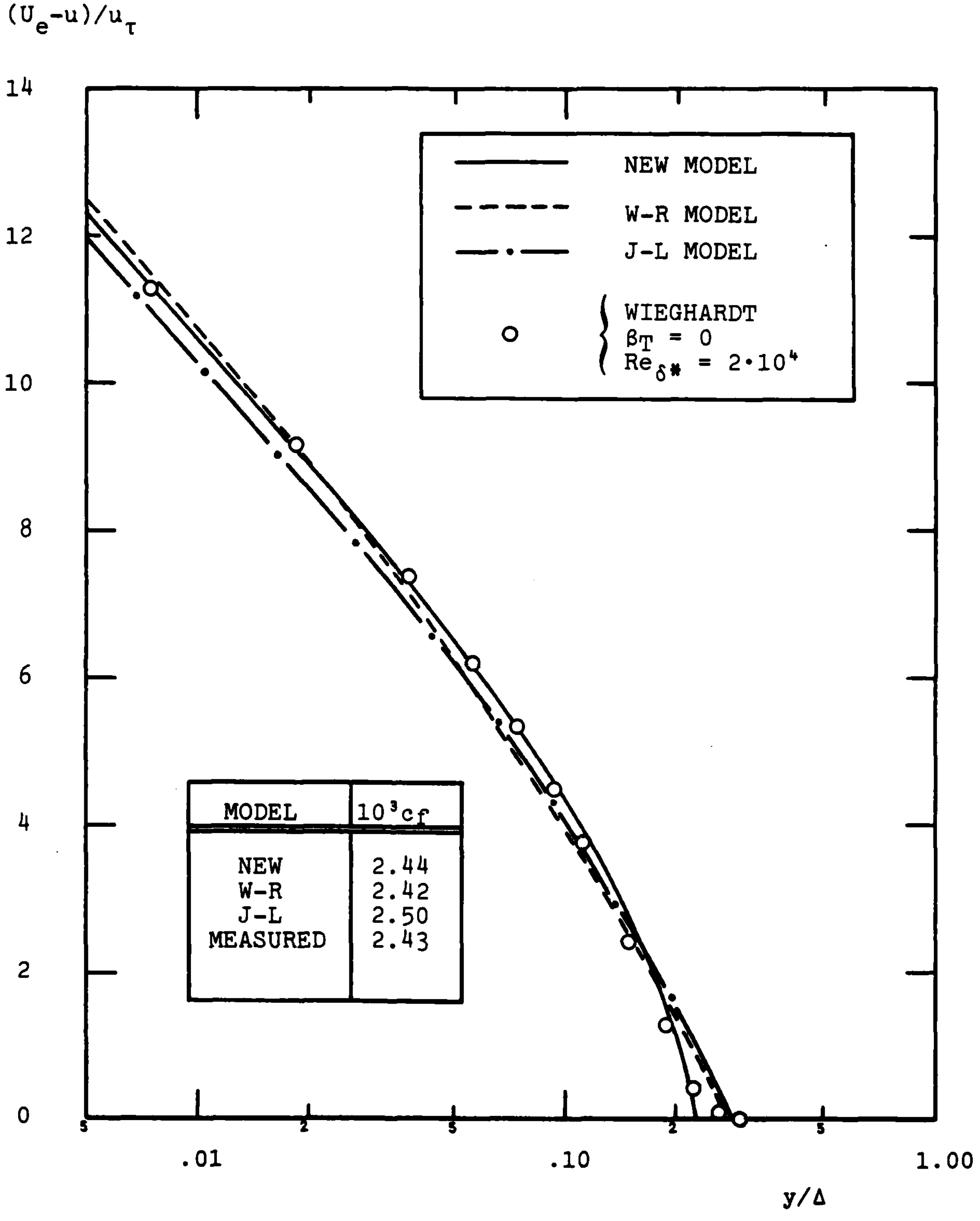

MODEL	$10^3 c_f$
NEW	2.44
W-R	2.42
J-L	2.50
MEASURED	2.43

Figure 1. Comparison of computed and measured velocity profiles in defect-layer coordinates for a constant-pressure boundary layer.

by the requirement of the perturbation solution that β_T be constant. This is as wide a range as we have been able to find for which experimental data have been taken with β_T more-or-less constant.

Figure 2 compares computed wake strength, $\tilde{\pi}$, with values inferred by Coles and Hirst from experimental data. For the sake of clarity, note that the wake strength appears in Cole's composite law-of-the-wall/wake profile, viz,

$$\frac{u}{u_\tau} = \frac{1}{\kappa} \ln\left[\frac{u_\tau y}{\nu}\right] + B + \frac{2\tilde{\pi}}{\kappa} \sin^2\left[\frac{\pi}{2} \frac{y}{\delta}\right] \qquad (19)$$

Appendix A summarizes the method used to infer $\tilde{\pi}$ from the numerical predictions.

Inspection of Figure 2 reveals provocative differences amongst the three models. Most notably, the new model yields wake strengths closest to values inferred from data over the complete range considered. Consistent with predictions of Chambers and Wilcox (Ref 15), the Jones-Launder model exhibits the largest differences, with predicted wake strength 50%-100% lower than inferred values when β_T is as small as two!

Figure 3 compares computed velocity profiles for $\beta_T = 9$ with experimental data of Clauser (Ref 2) for $\beta_T = 8.7$. As with the constant pressure case, computed and measured skin friction are included in the insert. Consistent with the wake-strength predictions, the new model yields a velocity profile and skin friction closest to measurements while the Jones-Launder model shows the greatest differences. The Wilcox-Rubesin profile and skin friction lie about midway between those of the other two models. Using Clauser's value for displacement-thickness Reynolds number, the velocity profiles are replotted in sublayer coordinates in Figure 4. As shown, differences amongst the models are as pronounced in sublayer coordinates as they are in defect-layer coordinates.

The explanation of the Jones-Launder model's poor performance for adverse pressure gradient can be developed from inspection of the asymptotic behavior of solutions as $\eta \rightarrow 0$. For the three models tested, the velocity behaves as follows.

$$\frac{U_e - u}{u_\tau} \rightarrow -\frac{1}{\kappa} \ln\eta + A - \beta_T B \eta \ln\eta + \ldots \qquad (20)$$

where the constants A and B are summarized in Table 1. Note that, while the coefficient A is determined as part of the solution (from the integral constraint that mass be conserved), the coefficient B follows directly from the limiting form of the solution as $\eta \rightarrow 0$. As seen from Table 1, B is largest for the Jones-Launder model and

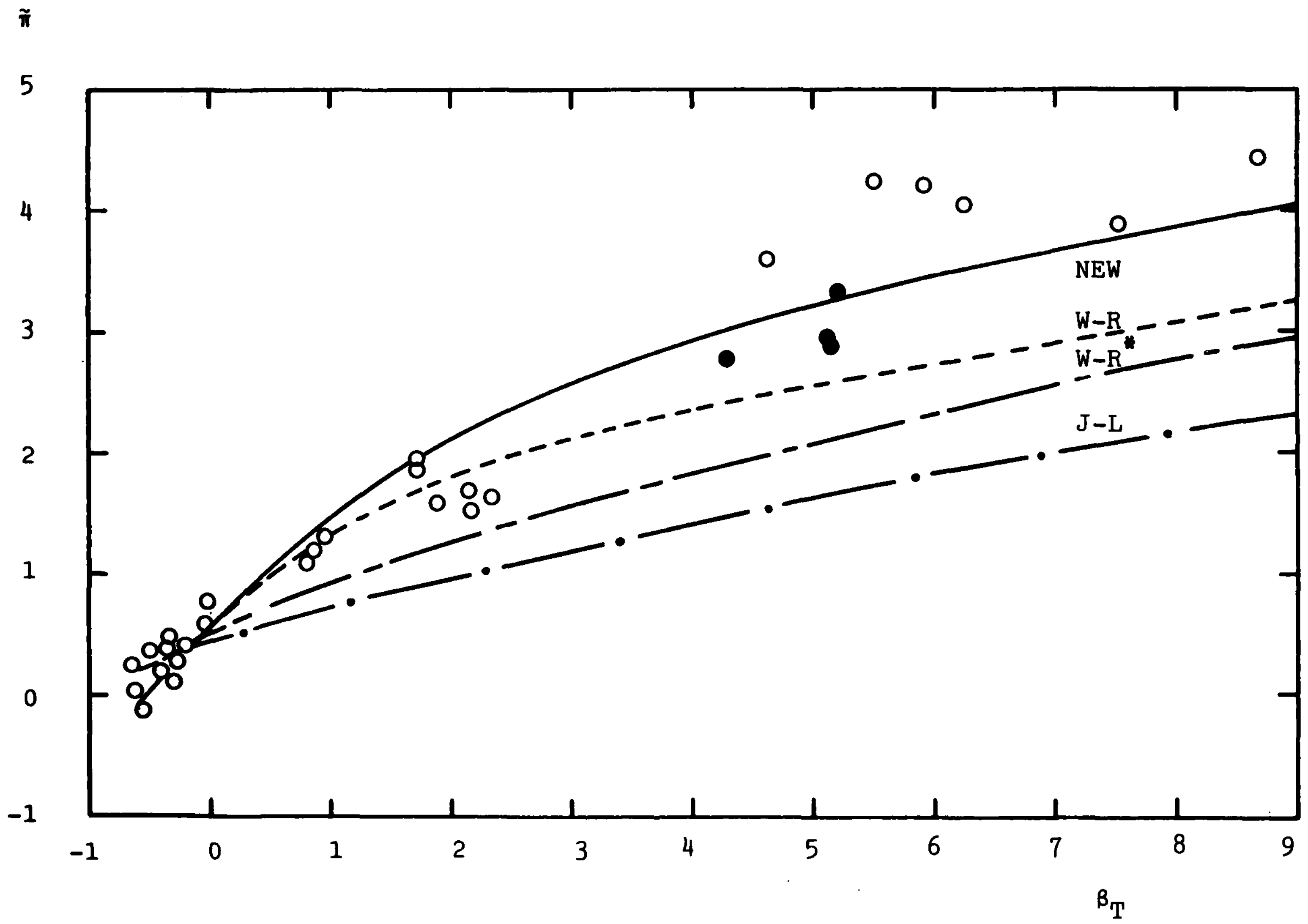

Figure 2. Comparison of computed and measured wake strength for equilibrium boundary layers with pressure gradient.

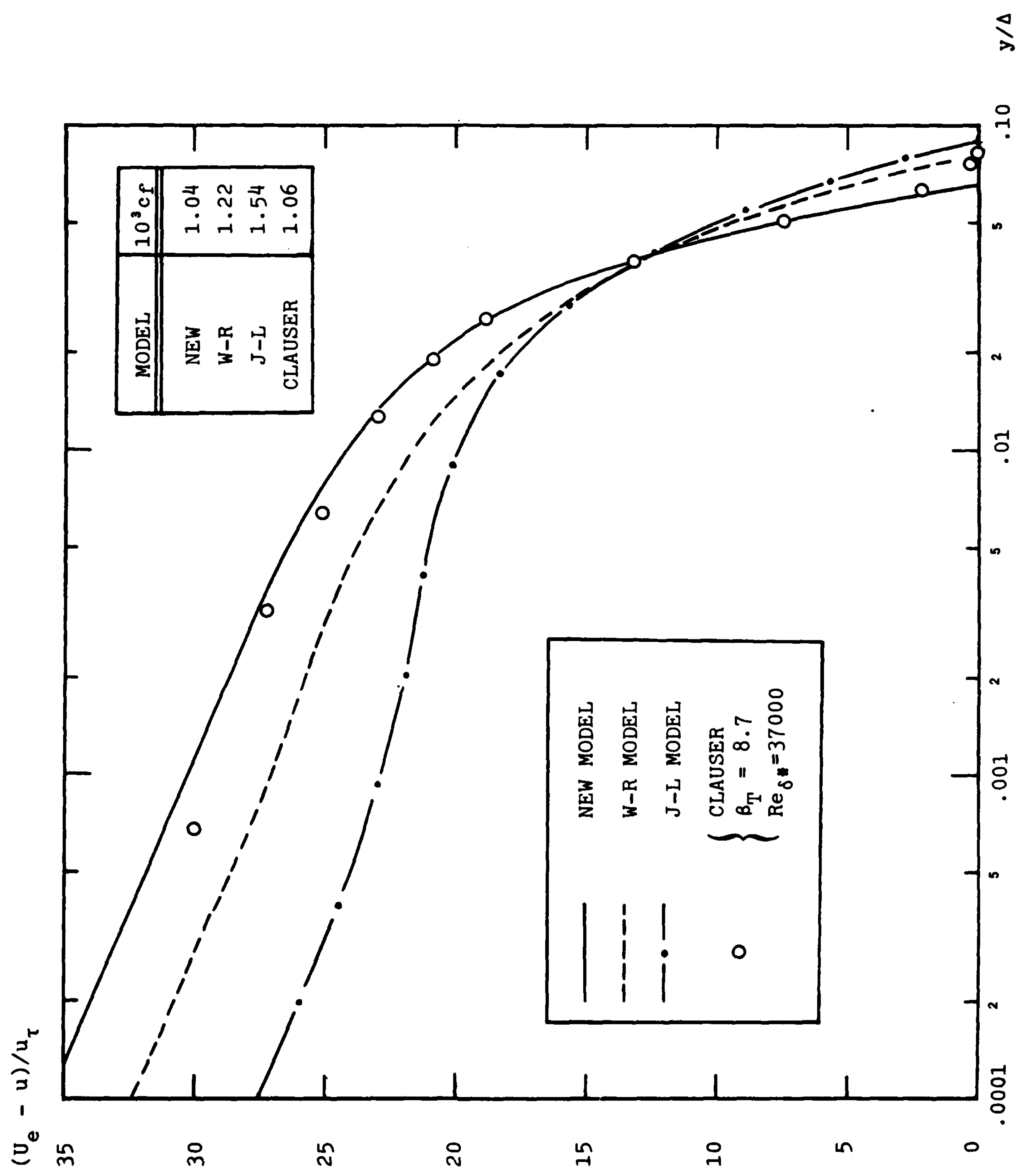

Figure 3. Comparison of computed and measured velocity profiles in defect-layer coordinates for $\beta_T = 9$.

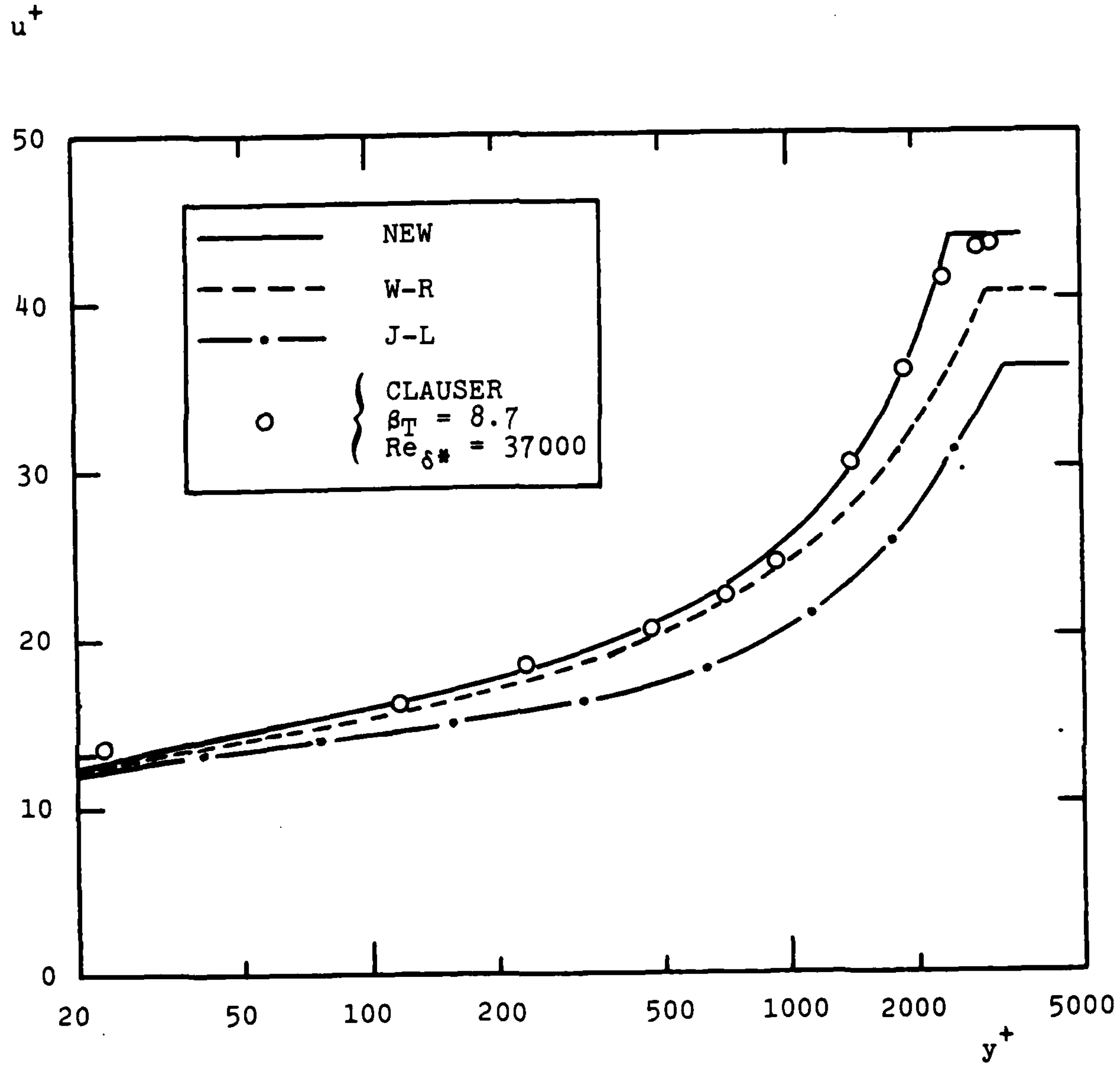

Figure 4. Comparison of computed and measured velocity profiles in sublayer coordinates for $\beta_T = 9$.

Table 1. Summary of Coefficients A, B and L in Equations (20-21) for β_T=9.

Model	A	B	L
New	13.1	10.6	-19.8
Wilcox-Rubesin	9.8	23.4	-32.6
Jones-Launder	5.4	54.8	-61.1

is smallest for the New model. The presence of the $\eta \ell n \eta$ term gives rise to the inflection in the velocity profile as $\eta \to 0$ that is most pronounced for the Jones-Launder model. In terms of turbulence properties, the turbulence length scale, $\ell = k^{1/2}/\omega = \beta^* k^{3/2}/\varepsilon$, behaves according to:

$$\ell \to \beta^{*1/4} \kappa \eta \left[1 + \beta_T L \eta \ell n \eta + \ldots \right] \tag{21}$$

where the coefficient L is summarized in Table 1. Again, we see that the contribution of the $\eta \ell n \eta$ term is largest for the Jones-Launder model and smallest for the New model. Thus, in the presence of adverse pressure gradient, the Jones-Launder ℓ tends to be too large in the near-wall region. Note, of course, that this shortcoming is not evident in the constant-pressure case which has $\beta_T = 0$.

The manner in which the New model achieves smaller values of ℓ than does the Jones-Launder model can be seen by changing dependent variables. That is, starting from the $k - \omega$ formulation and defining $\varepsilon = \beta^* k \omega$, we can deduce the following equation for ε implied by the New model.

$$\frac{d\varepsilon}{dt} = (1+\gamma) k \left[\frac{\partial u}{\partial y}\right]^2 - (1+\beta/\beta^*) \frac{\varepsilon^2}{k} + \frac{\partial}{\partial y}\left[\sigma \nu_T \frac{\partial \varepsilon}{\partial y}\right] - 2\sigma \nu_T \frac{\partial k}{\partial y} \frac{\partial (\varepsilon/k)}{\partial y} \tag{22}$$

All but the last term on the right-hand side of Equation (22) are identical in form to those of the Jones-Launder model (see Appendix A). The last term is negligibly small as $\eta \to 0$ for constant-pressure boundary layers because $k \to$ constant as $\eta = y/\Delta \to 0$. However, $\partial k/\partial y$ is nonvanishing when $\beta_T \neq 0$ and $\partial(\varepsilon/k)/\partial y$ generally is quite large as $\eta \to 0$. The net effect of this additional term is to suppress the rate of increase of ℓ close to the surface.

As a final comment, note that all of our computations have used the model-predicted behavior (e.g., Equations 20-21) as "wall-function" type boundary conditions for $\eta \to 0$. Using other empirical wall functions presumably would improve Jones-Launder predictions. However, the asymptotic behavior (e.g., inflected velocity profile) inherent to the model ultimately must prevail at high Reynolds number if the point of application of the wall functions remains constant at, say, $y^+ = 80$. To understand this point, one need only note that, by definition, η is related to y^+ by:

$$\eta = y^+ / Re_{\delta *} \tag{23}$$

Hence, suppressing the asymptotic behavior inherent to the model would require using wall functions to increasingly larger values of y^+ as Reynolds number increases.

3.4 ESTABLISHING CLOSURE COEFFICIENT VALUES

Unlike the four closure coefficients discussed in Subsection 2.2, we have been unable to find satisfactory arguments to establish the values of σ and σ^* prior to performing any numerical computations. However, we have found from numerical experimentation that computed variation of $\tilde{\pi}$ with β_T (Figure 2) seems to match experimental results most faithfully when we use $\sigma = \sigma^* = 1/2$. Effects of departures from this pair of values are so pronounced, in fact, that our computations seem to indicate $\sigma = \sigma^* = 1/2$ represents a saddle point in closure-coefficient space! Thus, we conclude that σ and σ^* are equal and the most appropriate value is 1/2.

4. SUBLAYER ANALYSIS

In order to facilitate integration of the model equations through the viscous sublayer, we must, at a minimum, add molecular diffusion terms to the equations of motion. Potentially, we might also have to allow the various closure coefficients to be functions of viscosity as well. In this section, we use perturbation methods to analyze viscous sublayer structure predicted by the new model, including effects of surface roughness and surface mass injection. Note that we confine our analysis to the new model as results of Section 3 indicate it is superior to the other models considered.

4.1 PERTURBATION SOLUTION

Considering the constant-pressure case only, convective terms are negligible in the sublayer; thus, the equations of motion for the new model (with molecular diffusion included) simplify to:

$$(\nu+\nu_T)du/dy = u_\tau^2 \tag{24}$$

$$\nu_T(du/dy)^2 - \beta^* k\omega + (d/dy)\left[(\nu+\sigma^*\nu_T)dk/dy\right] = 0 \tag{25}$$

$$\gamma(du/dy)^2 - \beta\,\omega^2 + (d/dy)\left[(\nu+\sigma\,\nu_T)d\omega/dy\right] = 0 \tag{26}$$

Five boundary conditions are needed, two of which follow from matching to the law of the wall as $y^+ \to \infty$, viz,

$$k \to u_\tau^2/\sqrt{\beta^*} \quad \text{and} \quad \omega \to u_\tau/\sqrt{\beta^*}\kappa y \quad \text{as} \quad y^+ \to \infty \tag{27}$$

Two more boundary conditions follow from "no slip" at the surface which implies that u and k vanish at y = 0. Thus,

$$u = k = 0 \quad \text{at} \quad y^+ = 0 \tag{28}$$

The final condition is similar to that deduced in earlier studies (Refs 7-9) where we have found that for perfectly-smooth surfaces molecular diffusion and dissipation balance in Equation (26) and this leads to:

$$\omega \to 6\nu/\beta y^2 \quad \text{as} \quad y^+ \to 0 \tag{29}$$

More general boundary conditions for rough surfaces and for surfaces with mass injection will be devised in Subsections 4.2-4.3. For now, we focus on the perfectly-smooth surface.

As part of the solution to Equations (24-29), we obtain the constant in the law of the wall, B, where

$$u^+ \to \frac{1}{\kappa} \ln y^+ + B \quad \text{as} \quad y^+ \to \infty \tag{30}$$

We solve the sublayer equations by: (a) adding unsteady terms to the right-hand sides of Equations (25-26); (b) making an initial guess of the solution; and (c) using an implicit, time-marching, second-order-accurate program to generate the long-time solution in which the unsteady terms tend to zero. The velocity is computed at each timestep using the fourth-order Runge-Kutta method. The program used is an improved version of that developed in the study by Wilcox and Traci (Ref 8).

Using this program, we find that Equations (24-29) predict that the smooth-wall value of B is

$$B = \lim_{y^+ \to \infty} \left[u^+ - \frac{1}{\kappa} \ln y^+ \right] \approx 5.1 \tag{31}$$

The fact that this value is well within the scatter of measured values of B strongly suggests that no further viscous modifications are needed for this model.

Figures 5 and 6 compare computed and measured (Refs 2,16,17) sublayer velocity profiles in linear and semilog coordinates. The two figures show that computed velocities generally fall within experimental data scatter. In Figure 7, we compare computed and measured turbulence production and dissipation terms. Again, predictions fall well within experimental error bounds.

Perhaps the only deficiency of the predicted smooth-surface sublayer structure is that very near the surface the model predicts

$$k \sim y^{3.23} \quad \text{as} \quad y \to 0 \tag{32}$$

By contrast, the Wilcox-Rubesin model predicts that $k \sim y^4$ which suggests that $k \sim \langle v'^2 \rangle$, a point this researcher has made as a more physically plausible interpretation than saying k is the kinetic energy of the turbulence. By letting the closure coefficient β^* increase as a function of turbulent Reynolds number, Re_T defined as $k/\omega\nu$, it is possible to force $k \sim y^4$ but then we find that to recover $B = 5$, at least two other closure coefficients must vary with Re_T (see Appendix B). Such additional complexity is pointless in light of Figures 5 through 7.

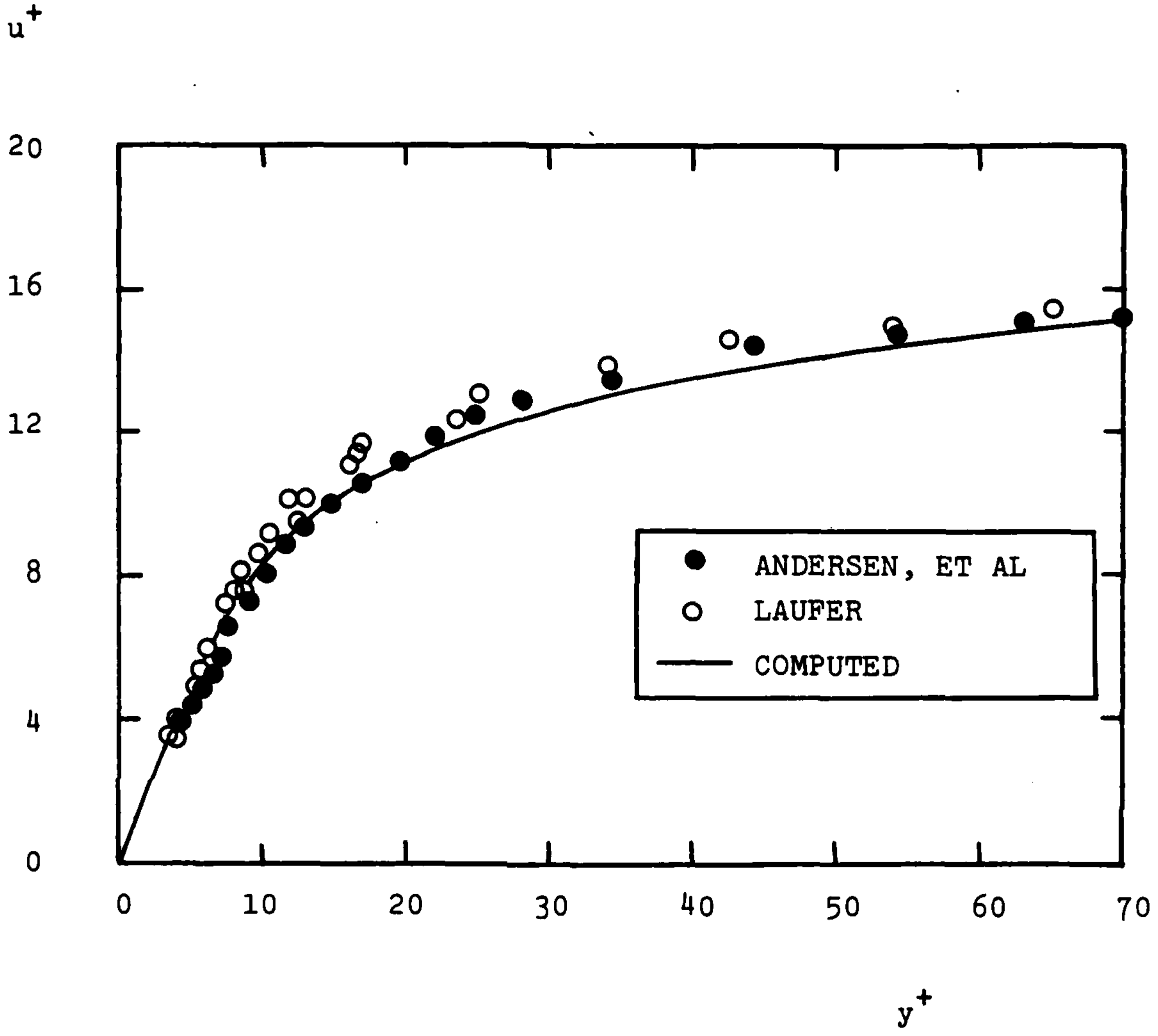

Figure 5. Comparison of computed and measured near-surface velocity profiles for a boundary layer over a perfectly-smooth surface.

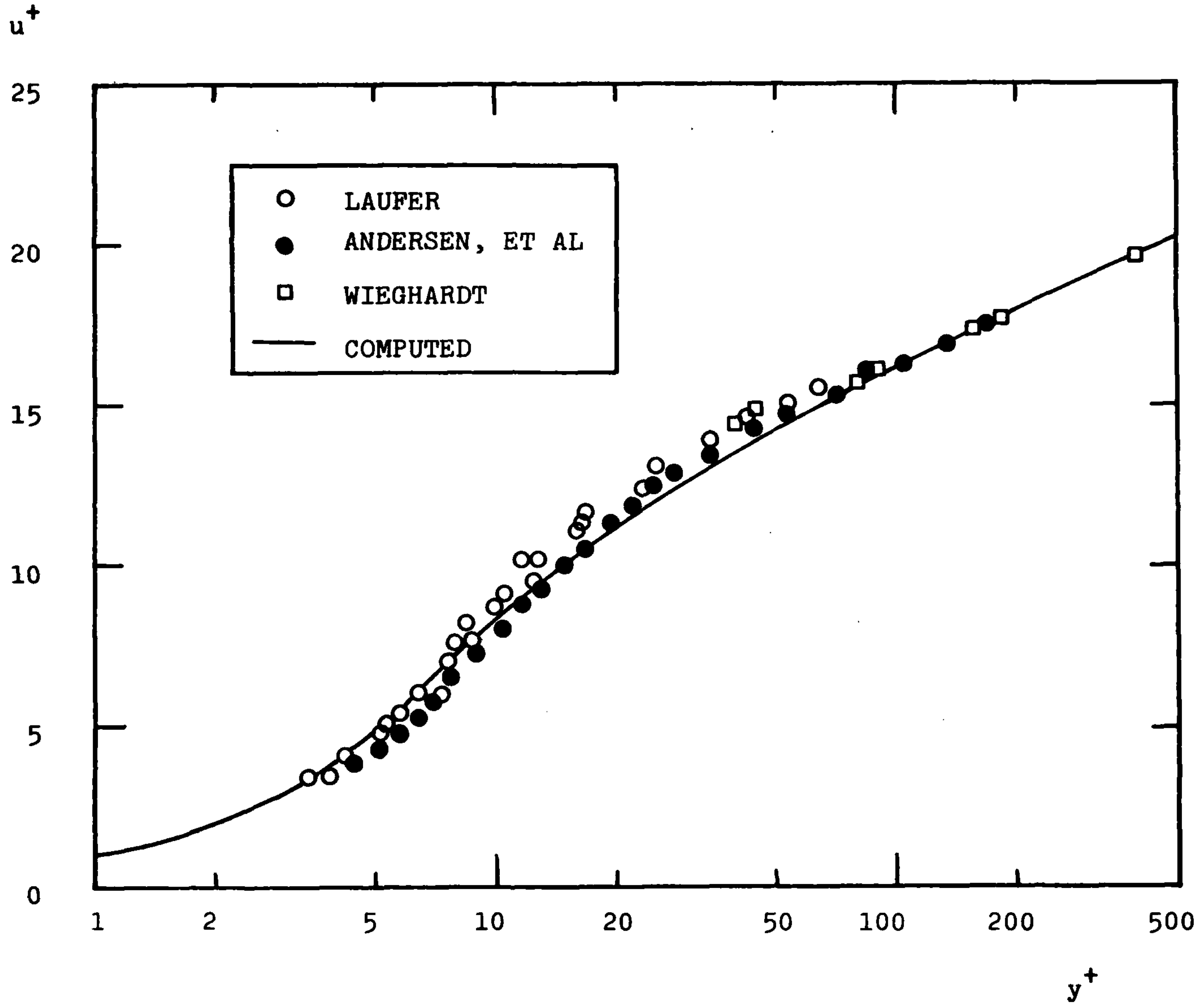

Figure 6. Comparison of computed and measured velocity profiles in sublayer coordinates; sublayer perturbation analysis.

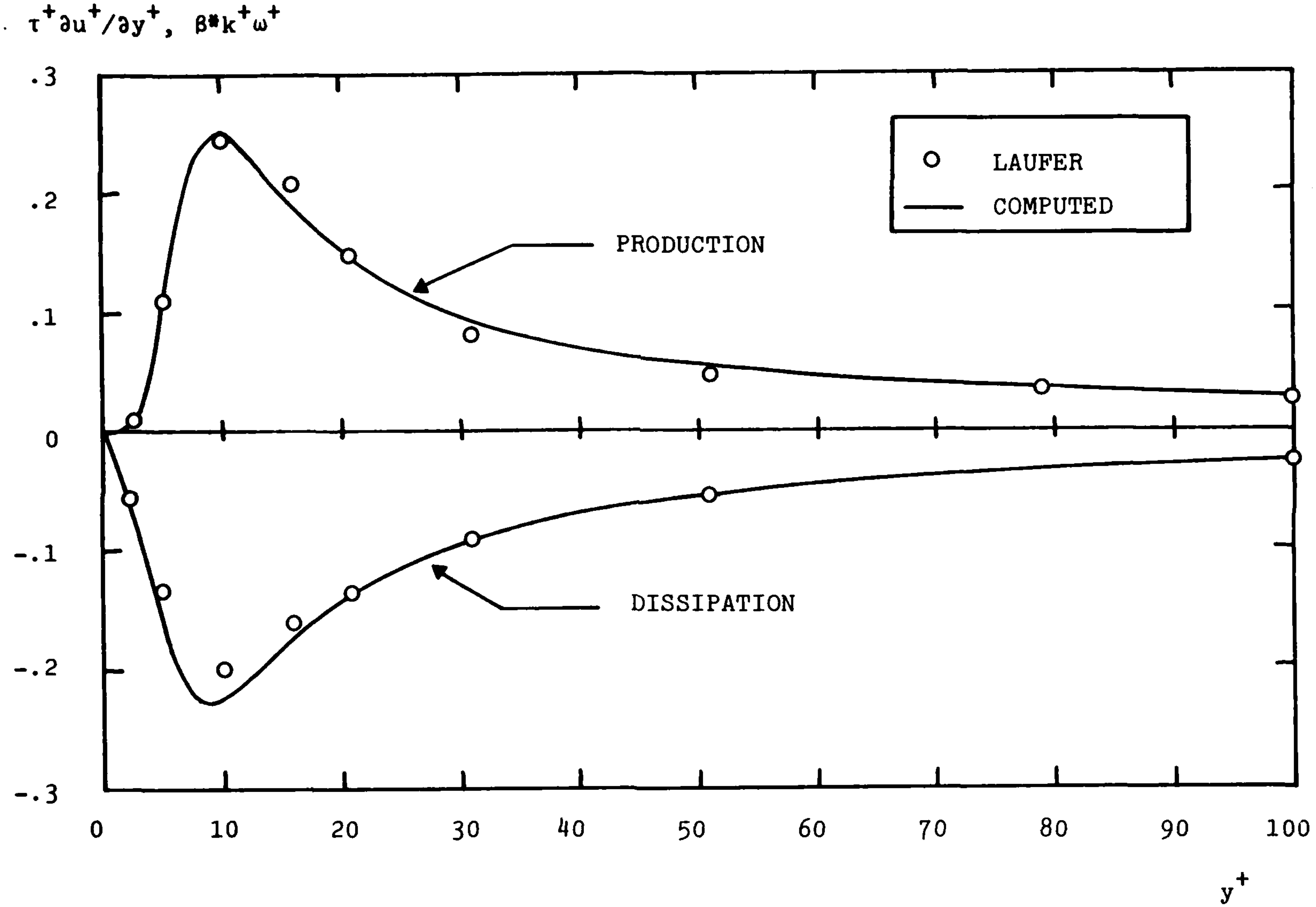

Figure 7. Comparison of computed and measured near-surface turbulent-energy production and dissipation.

4.2 ROUGH-WALL ANALYSIS

A key advantage of the $k-\omega^2$ and $k-\omega$ formulations over the $k-\varepsilon$ formulation is the fact that ω-oriented equations possess solutions in which the value of ω may be arbitrarily specified at the surface (Ref 15). This is an advantage because it provides a natural way to incorporate effects of surface roughness through surface boundary conditions. This feature of the equations was originally recognized by Saffman (Ref 18).

If we now rewrite the surface boundary condition (Equation 29) on ω as follows,

$$\omega = \frac{u_\tau^2}{\nu} S_R \qquad \text{at} \qquad y = 0 \tag{33}$$

we can generate sublayer solutions for arbitrary S_R, including the limiting cases $S_R \to 0$ and $S_R \to \infty$.

Figure 8 shows the computed value of B for a wide range of values of S . As shown, in the limit $S_R \to \infty$, B tends to 5.1. To determine the limiting value of B as S_R becomes small, we replot the numerical results on semilog paper in Figure 9. As shown, an excellent correlation of the numerical predictions is given by:

$$B \to 8.4 + \frac{1}{\kappa} \ln(S_R/100) \qquad \text{as} \qquad S_R \to 0 \tag{34}$$

By experimental means, Nikuradse (Ref 19) has found that for flow over very rough surfaces:

$$B \to 8.5 + \frac{1}{\kappa} \ln(1/k_R^+) \qquad ; \qquad k_R^+ = u_\tau k_R/\nu \tag{35}$$

where k_R is the average height of sand-grain roughness elements. (Note that in our computations we use $\kappa = 0.41$ while Nikuradse used $\kappa = 0.40$.) Thus, if we make the correlation:

$$S_R = 100/k_R^+ \qquad ; \qquad k_R^+ \gg 1 \tag{36}$$

then Equations (34) and (35) are nearly identical. Figure 10 compares computed velocity profiles with the analytical fit obtained by using Equations (34-35) in the law of the wall, viz,

$$u^+ = \frac{1}{\kappa} \ln(y/k_R) + 8.4 \tag{37}$$

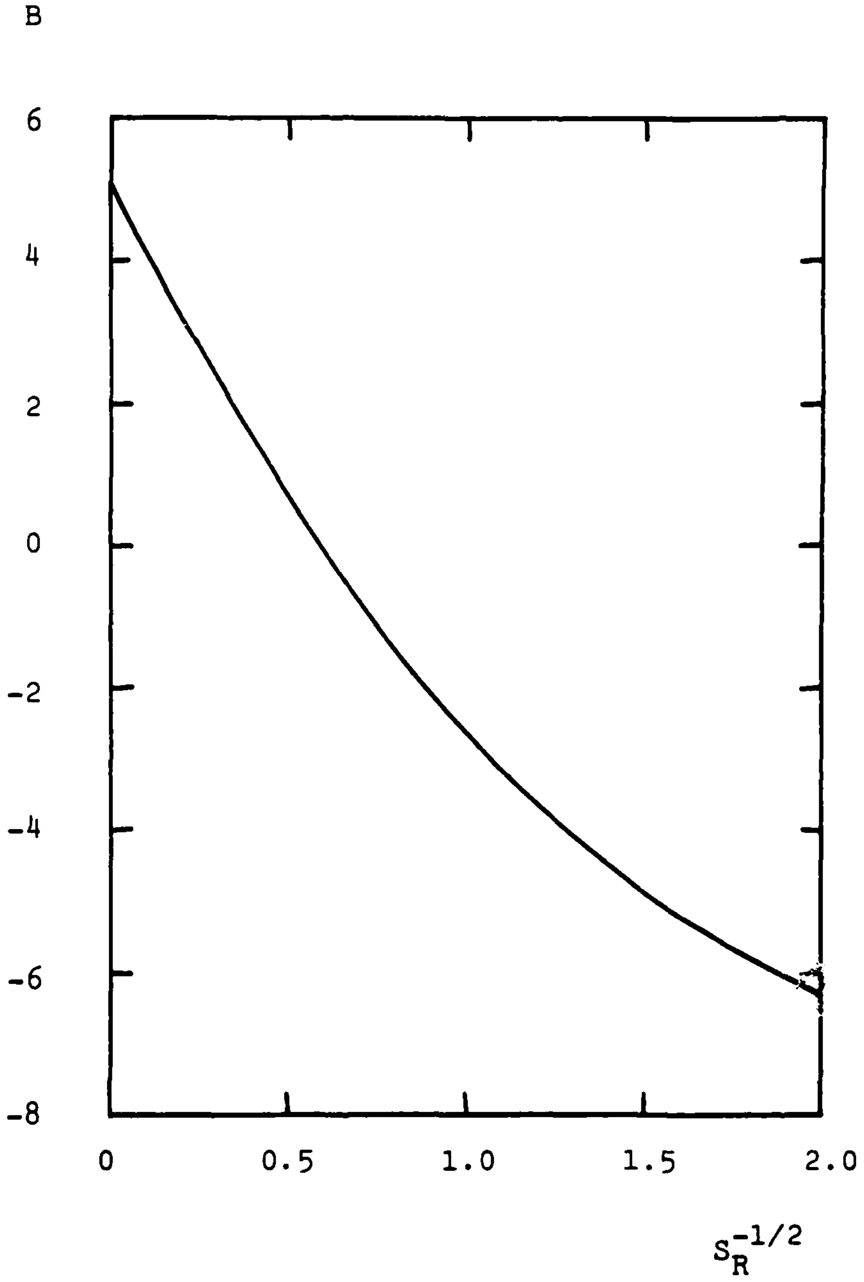

Figure 8. Computed variation of the constant in the law of the wall, B, with the surface value of the dissipation rate.

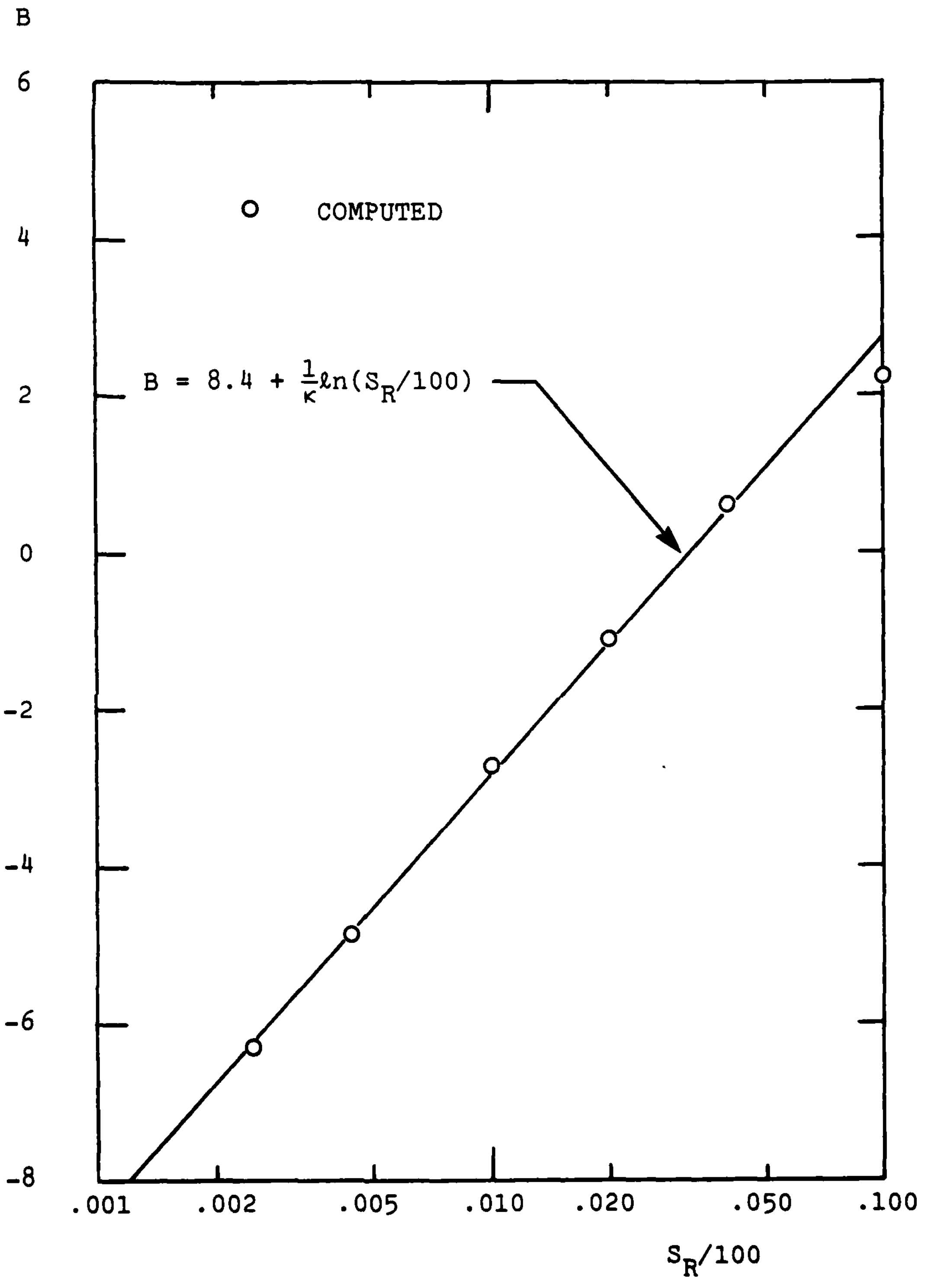

Figure 9. Asymptotic behavior of the computed constant in the law of the wall, B, for small S_R.

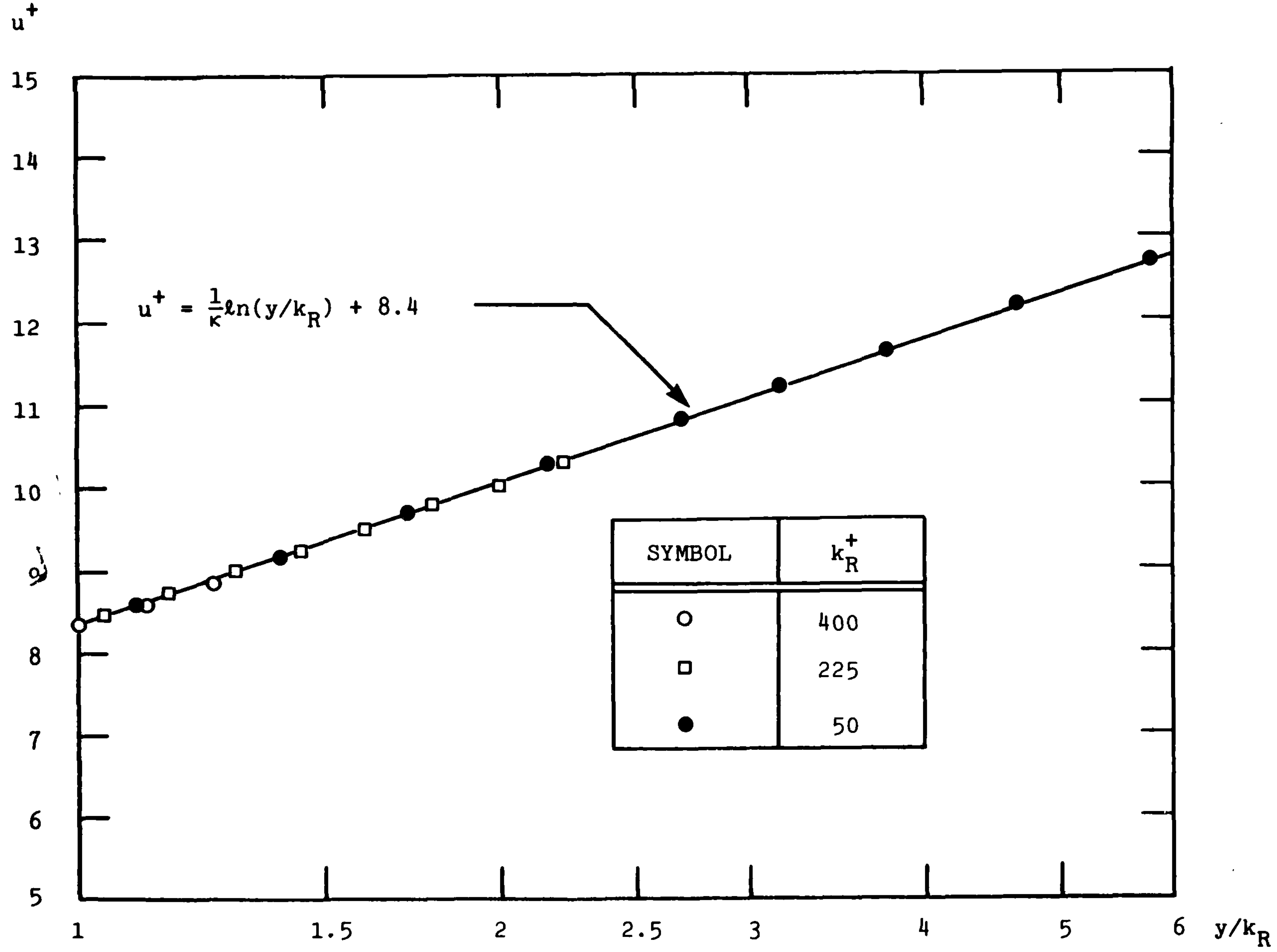

Figure 10. Computed velocity profiles for "completely-rough" surfaces.

for three of the computations. The correlation is nearly exact. The most remarkable fact about this correlation is that Equation (37) is the form the law of the wall assumes for flow over "completely-rough" surfaces, including the value of the additive constant (8.4 and 8.5 differ by one percent).

By making a qualitative argument based on flow over a wavy wall, Wilcox and Chambers (Ref 20) have shown that for small roughness heights, we should expect to have

$$S_R \sim (1/k_R^+)^2 \qquad ; \qquad k_R^+ \to 0 \tag{38}$$

Comparison with Nikuradse's data (Figure 11) shows that the following correlation between S_R and k_R^+ will reproduce measured effects of sand-grain roughness for values of k_R^+ up to about 400.

$$S_R = \begin{cases} (50/k_R^+)^2 & ; \quad k_R^+ < 25 \\ 100/k_R^+ & ; \quad k_R^+ > 25 \end{cases} \tag{39}$$

4.3 EFFECTS OF SURFACE MASS INJECTION

For boundary layers with surface mass injection, the introduction of an additional velocity scale (v_w = normal flow velocity at the surface) suggests that the scaling for ω at the surface may differ from Equation (33). Andersen, et al (Ref 17) provide further evidence that the dissipation-rate boundary condition must be revised when mass injection is present by showing, from correlation of their experimental data, that both κ and B are functions of $v_w^+ = v_w/u_\tau$. Because our rough-surface computations of the preceding subsection show that the value of B is strongly affected by the surface value of the dissipation rate, this suggests that the surface value of ω will depend in some manner upon v_w^+ . Examination of the limiting form of the model equations for $y^+ \to \infty$ (i.e., the "wall-layer"...Subsection 2.2) shows immediately that the effective Karman "constant" varies with v_w^+ according to:

$$\tilde{\kappa} = \kappa/(1 + \Xi\, v_w^+) \tag{40}$$

where Ξ is given by

$$\Xi = 3.11 + 0.61\, \ell n y^+ \tag{41}$$

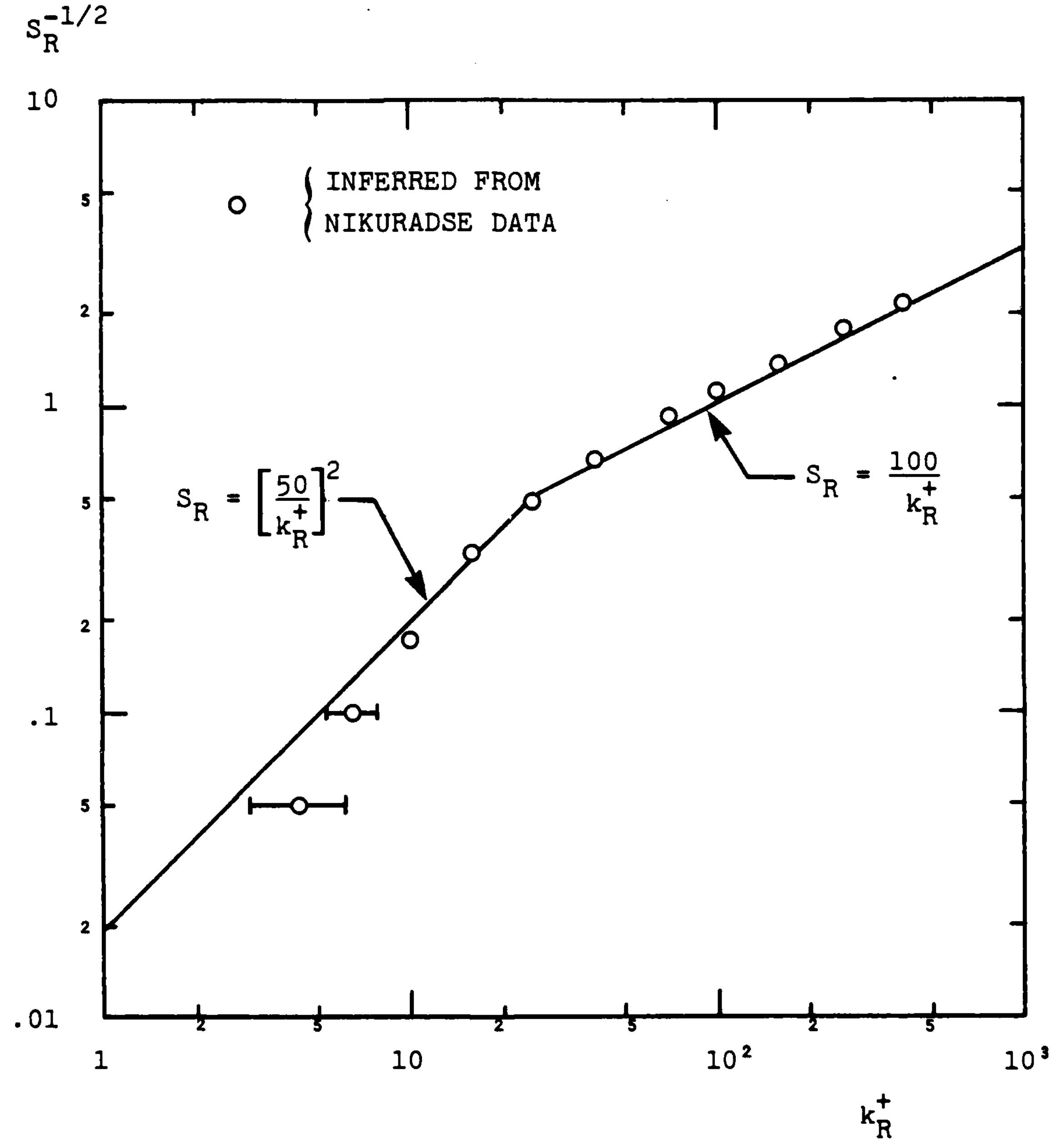

Figure 11. Correlation of S_R with roughness height, k_R^+.

The variation of $\tilde{\kappa}$ predicted in Equations (40-41) is consistent with the Andersen, et al data. Including appropriate convective terms in Equations (24-26), we have performed sublayer computations for the cases experimentally documented by Andersen, et al. In each case, the surface value of ω has been given by

$$\omega = \frac{u_\tau^2}{\nu} S_B \quad \text{at} \quad y = 0 \tag{42}$$

and the value of S_B has been varied until optimum agreement between measured and computed velocity profiles is achieved. The final correlation between S_B and v_w^+ is shown in Figure 12. The correlation is given in analytical form as:

$$S_B = \frac{20}{v_w^+(1+5v_w^+)} \tag{43}$$

Figure 13 displays the level of agreement between theory and experiment using Equations (42) and (43).

This concludes our formulation of the new turbulence model and attending surface boundary conditions. In the following section, we focus on application of the new model in several numerical computations.

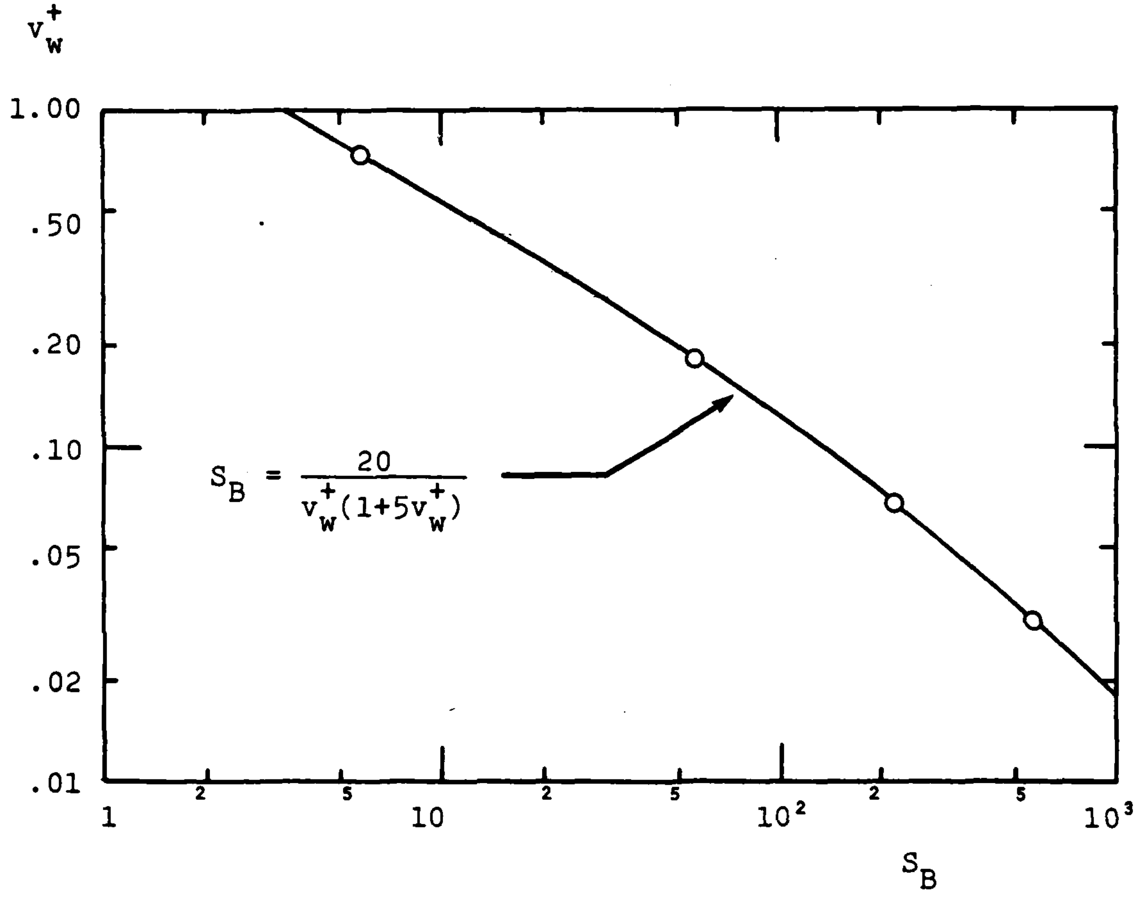

Figure 12. Correlation of S_B with blowing-rate, v_w^+.

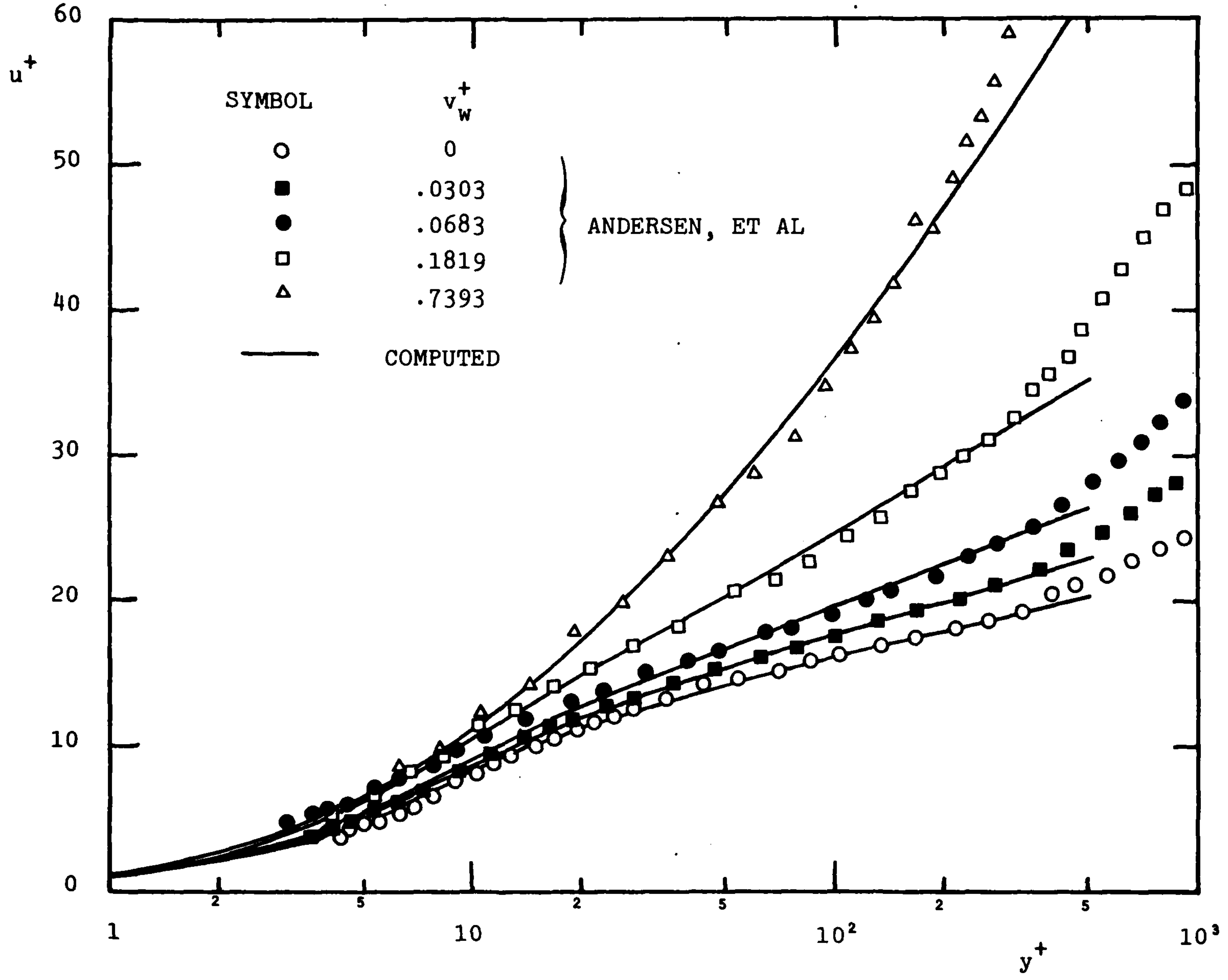

Figure 13. Comparison of computed and measured sublayer velocity profiles for boundary layers with mass injection.

5. BOUNDARY-LAYER APPLICATIONS

We turn now to application of the new model equations to a total of five incompressible boundary layers. First, we present details of the manner in which we determine boundary conditions for the turbulence-model parameters appropriate at the boundary-layer edge. Then we apply the model to the constant-pressure (flat-plate) case. The next two applications are to boundary layers in an adverse pressure gradient. The final two applications are for boundary layers with surface mass transfer. All computations have been done with the model as formulated in Sections 2 through 4 and, with the viscous modifications of Appendix B included. Graphical results are almost identical for each corresponding pair of computations. Thus, only one curve is presented for the flow properties displayed.

5.1 BOUNDARY-LAYER-EDGE CONDITIONS

While the preceding section discussed surface boundary conditions, we have not yet commented on boundary conditions appropriate in the freestream, or in the case of a boundary layer, at the edge of the layer. In prior computations with our two-dimensional boundary-layer program, EDDYBL (Ref 21), we have held the ratio of turbulent energy to the square of the mean edge velocity constant at the edge of the layer. Additionally, we have held the ratio of the turbulent length scale, $\ell = \sqrt{k}/\omega$, to the local boundary-layer thickness constant. These two boundary conditions are more-or-less consistent with our defect-layer analysis. However, in past studies, we have found that these boundary conditions can lead to numerical difficulties, particularly at high Reynolds numbers. In order to avoid these numerical difficulties in this study, we have adopted a different approach.

Ideally, we would like to implement "zero-gradient" boundary conditions at the boundary-layer edge. While such conditions are "clean" from a theoretical point of view, they are undesirable from a numerical point of view. That is, the conditions we have used in past applications are of the Neumann type while "zero-gradient" conditions are of the Dirichlet type. Almost universally, convergence of iterative numerical schemes (EDDYBL uses an iterative scheme) is much slower with Dirichlet conditions than with Neumann conditions.

In order to resolve this apparent dilema, we appeal directly to the equations of motion. Beyond the boundary-layer edge, we have vanishing normal gradients so that the equations for k and ω simplify to the following.

$$\left.\begin{aligned} U_e \, dk_e/dx &= -\beta^* \omega_e k_e \\ U_e \, d\omega_e/dx &= -\beta \, \omega_e^2 \end{aligned}\right\} \qquad (44)$$

where x is freestream flow direction, subscript e denotes the value at the boundary-layer edge, and β and β^* are defined in Equations (8). The solution to Equations (44) can be obtained by simple quadrature, independent of integrating the equations of motion through the boundary layer. Once k_e and ω_e are determined from Equations (44), it is then possible to specify Neumann-type boundary conditions which guarentee zero normal gradients.

Using boundary conditions based on quadrature of Equations (44), we have performed a series of numerical experiments to test solution sensitivity to the boundary conditions. In all of our tests, very little solution sensitivity is evident. Most importantly, the two turbulence parameters k and ω tend smoothly to their freestream values. By contrast, the boundary conditions we have used in past studies produce sharp turbulent-nonturbulent interfaces which sometimes hamper solution convergence. The new boundary conditions thus appear to be more satisfactory.

5.2 FLAT-PLATE BOUNDARY LAYER

Our first application is the constant-pressure (flat-plate) boundary layer. While this application does not provide a severe test of the new model, it is nevertheless necessary to be sure the boundary-layer program has been coded properly. Additionally, the new model wouldn't be of much use as a predictive tool if it were inaccurate for this simplest of all boundary layers.

The computation begins at a plate-length Reynolds number, Re_x, of one million and continues to an Re_x of 10.9 million. A total of 244 steps are taken in the streamwise direction. Grid points normal to the surface are spaced in a geometric progression with a grading ratio of 11%; the total number of points used to resolve the layer increases from 61 initially to 66 by the end of the computation (to accomodate boundary-layer growth). Numerical experimentation with the current version of EDDYBL (Ref 22) has shown that our solutions are grid independent for 60 mesh points. Accuracy to within 3 percent can be achieved with as few as 40 mesh points.

Figures 14 and 15 compare computed and measured skin friction and velocity profiles, respectively. As shown in Figure 14, computed skin friction virtually duplicates corresponding measurements for the entire range of Reynolds numbers considered. Figure 15 shows that differences between computed and measured velocity profiles are no more than 3 percent of scale for the three Reynolds numbers indicated.

Thus, as no great surprise, the new model is quite accurate for the flat-plate boundary layer. In the next two applications, we address boundary layers experiencing an adverse pressure gradient.

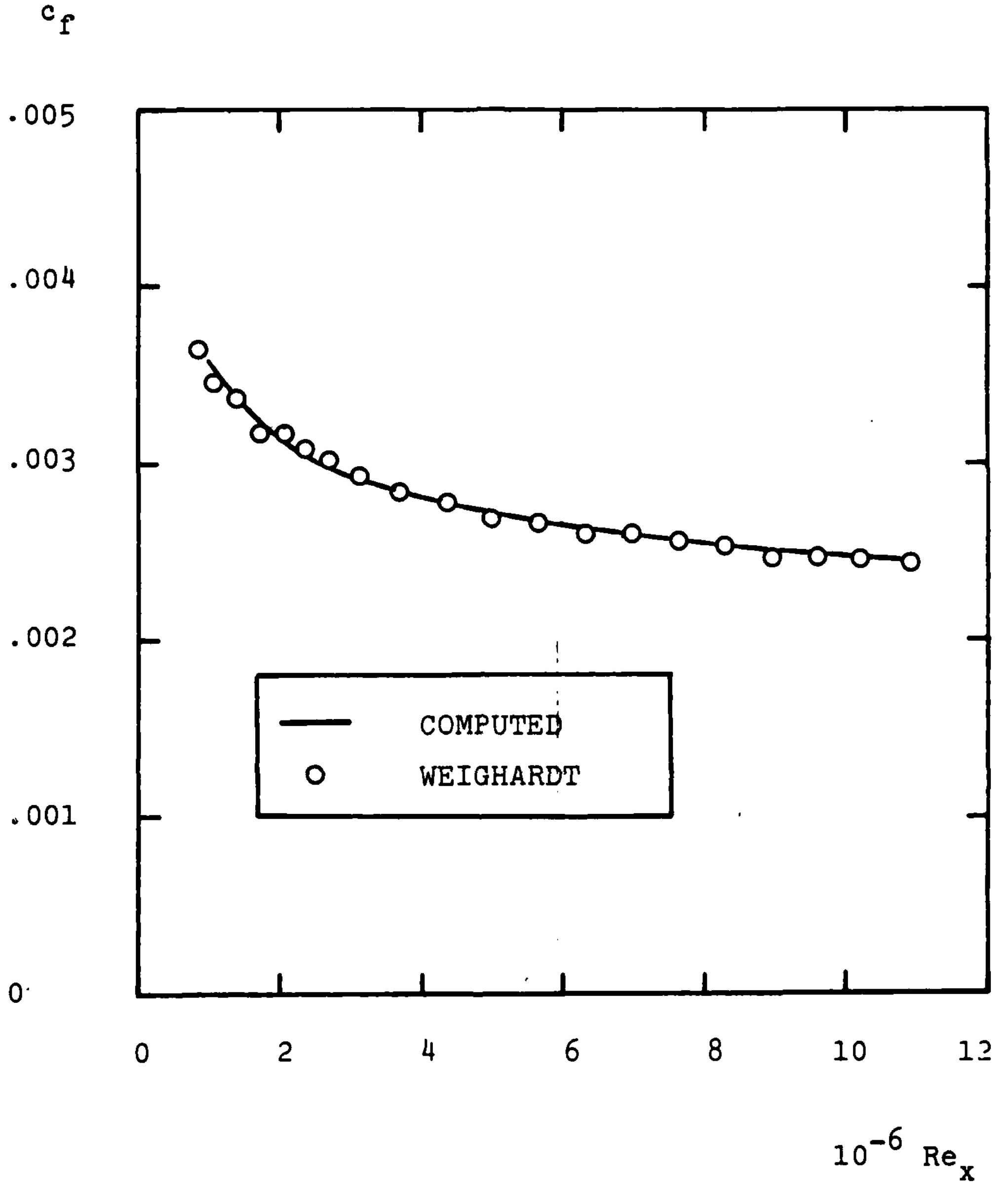

Figure 14. Comparison of computed and measured skin friction for a flat-plate boundary layer.

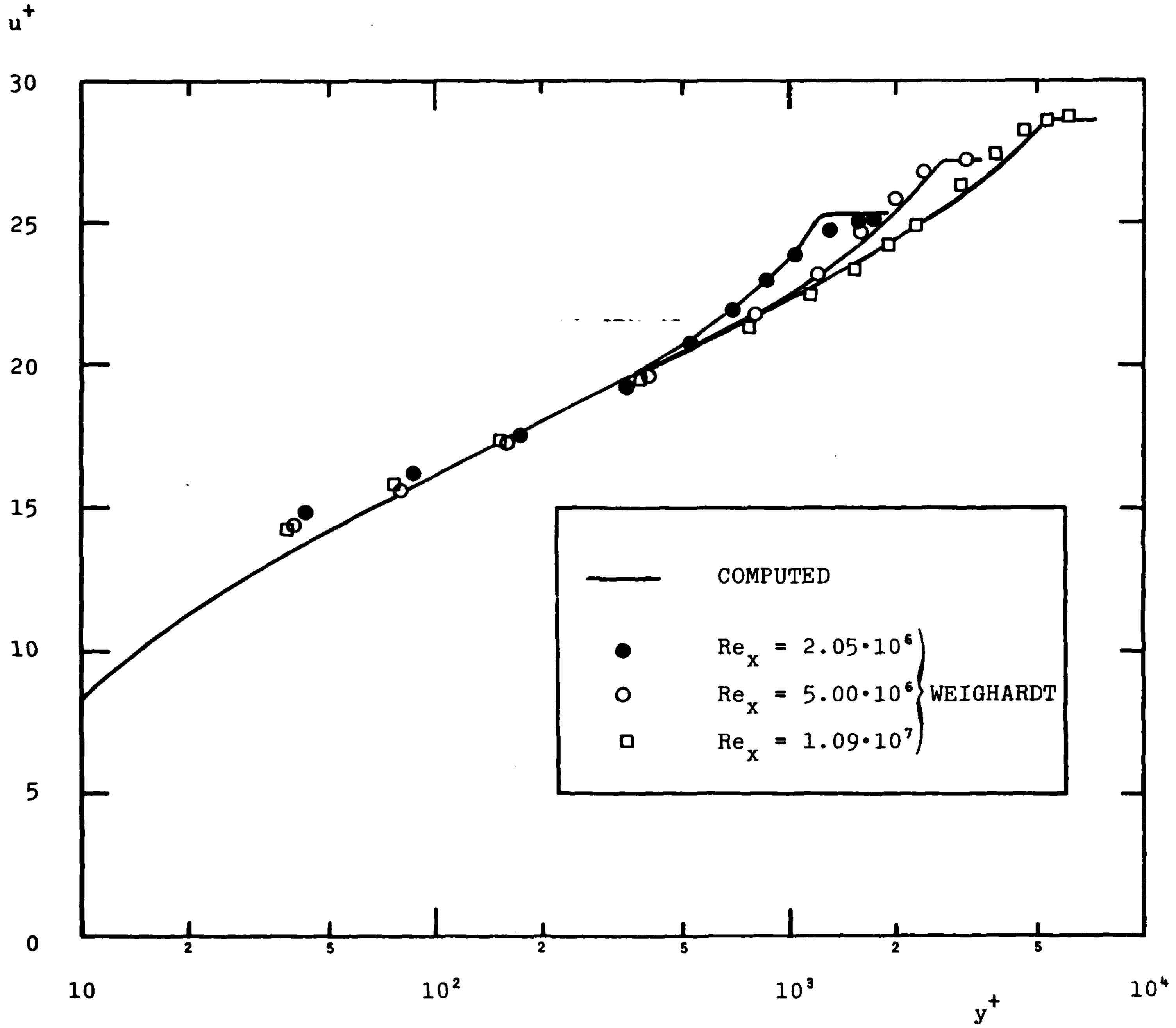

Figure 15. Comparison of computed and measured velocity profiles for a flat-plate boundary layer.

5.3 BOUNDARY LAYERS WITH ADVERSE PRESSURE GRADIENT

We consider two boundary layers with adverse pressure gradient. The first case has a moderate adverse pressure gradient, the experimental data being those of Bradshaw (Ref 2...Case 3300). The second case has increasingly adverse pressure gradient, the experimental data being those of Samuel and Joubert (Ref 10...Flow S2).

For the Bradshaw case, a total of 90 streamwise steps are needed to march from x = 2.5 ft to x = 7.0 ft, corresponding to Re_x increasing from about 2 million to about 4 million. A geometric-progression ratio of 13% is used to construct the grid normal to the surface with a total of 61 points throughout the computation.

Figures 16 and 17 compare computed and measured skin friction and a velocity profile. Inspection of both graphs shows that differences between theory and experiment nowhere exceed 5 percent for this flow.

In the Samuel-Joubert case, we use 100 streamwise steps to march from x = 1 m to x= 3.40 m, corresponding to an Re_x range of about 2 million to 4 million. To achieve an extremely accurate numerical solution in this case, we have used a geometric-progression ratio of 7.8% and a total of 81 mesh points. Results differ from a 61-point computation by less than a half a percent.

Figures 18 and 19 compare computed and measured skin friction and two velocity profiles for this flow. Computed and measured skin friction differ by less than 7 percent of scale. The velocity profiles at x = 2.87 m are within 5 percent while those at x = 3.40 m differ by no more than 9 percent. Although our predictions for this case differ from measurements a bit more than the other two cases, note that our predictions for this flow at the Second Stanford Olympiad typically differed from measurements by as much as 25 percent, and our prediction was one of the best submitted.

5.4 BOUNDARY LAYERS WITH SURFACE MASS TRANSFER

As our final two applications of the model, we consider two cases with surface mass transfer. Both cases were included in the 1981 Stanford Olympics (Ref 10) and data for both cases were taken by Andersen, et al (Ref 17). The first case has surface mass injection rate, v_w, given by $.00375\ U_e$. The second case has surface mass removal rate, v_w, given by $-.00375\ U_e$. For the blowing case pressure is constant, while the suction case has a slight adverse pressure gradient.

Figures 20 and 21 compare computed and measured skin friction and velocity profiles, respectively, for the blowing case. As shown, computed and measured skin friction differ by less than 4 percent

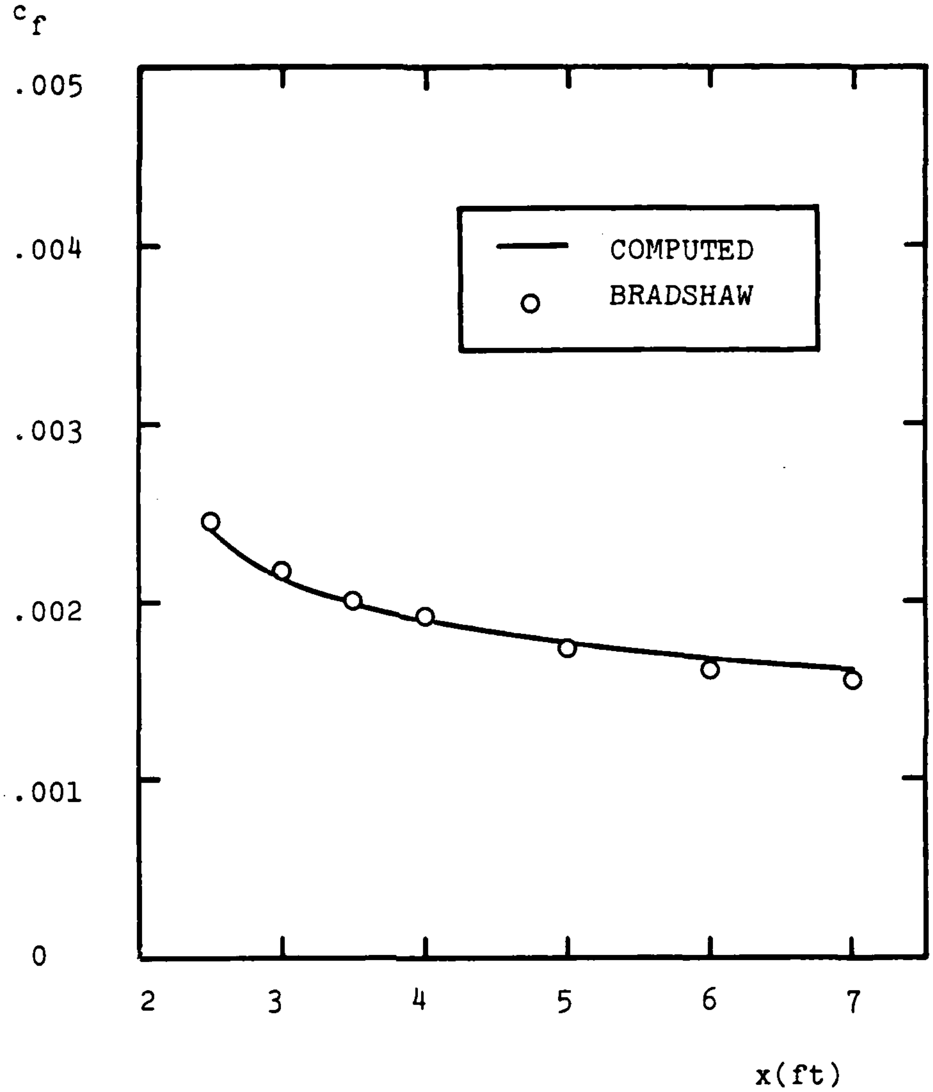

Figure 16. Comparison of computed and measured skin friction for Bradshaw's Flow C.

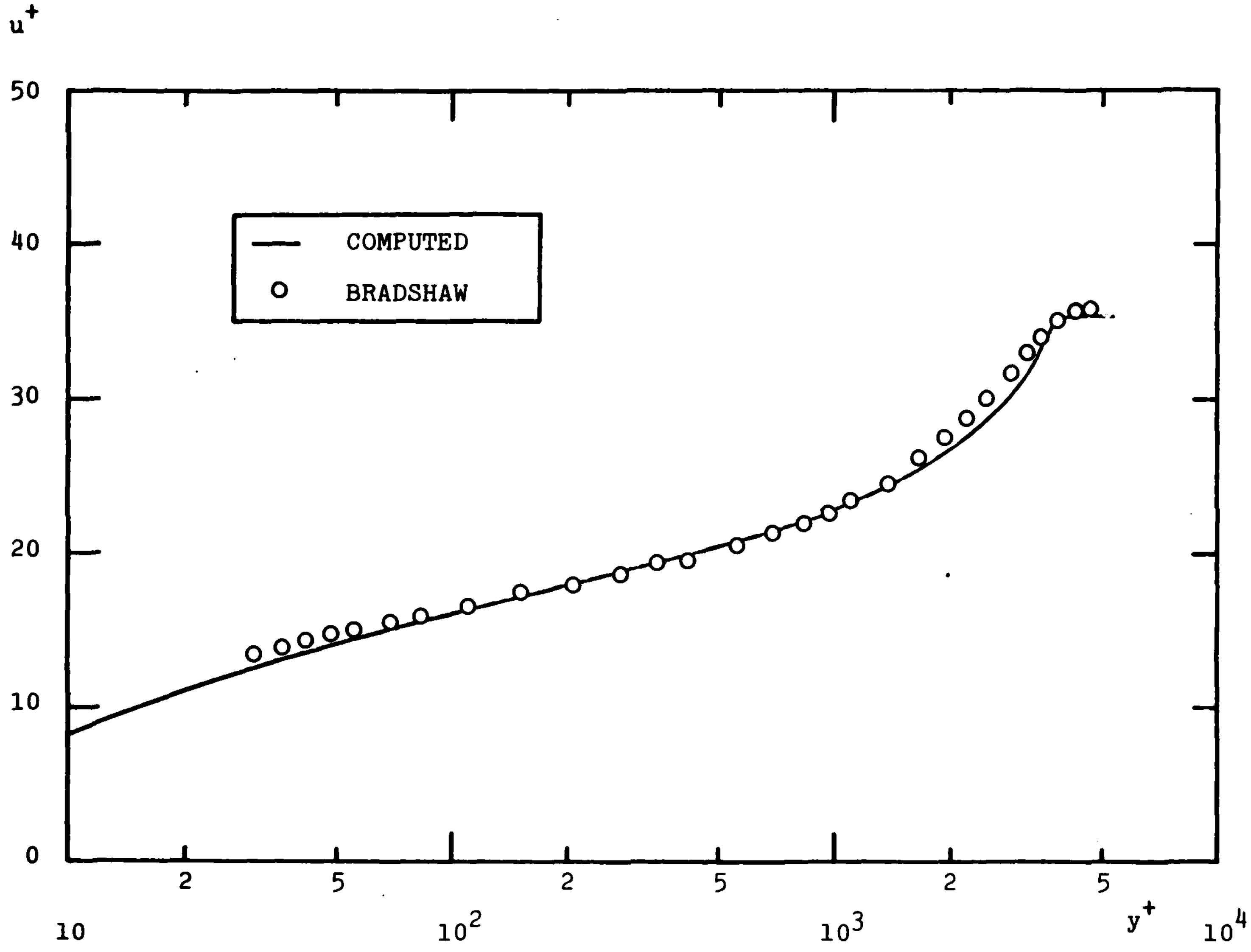

Figure 17. Comparison of computed and measured velocity profiles for Bradshaw's Flow C; x = 7 ft.

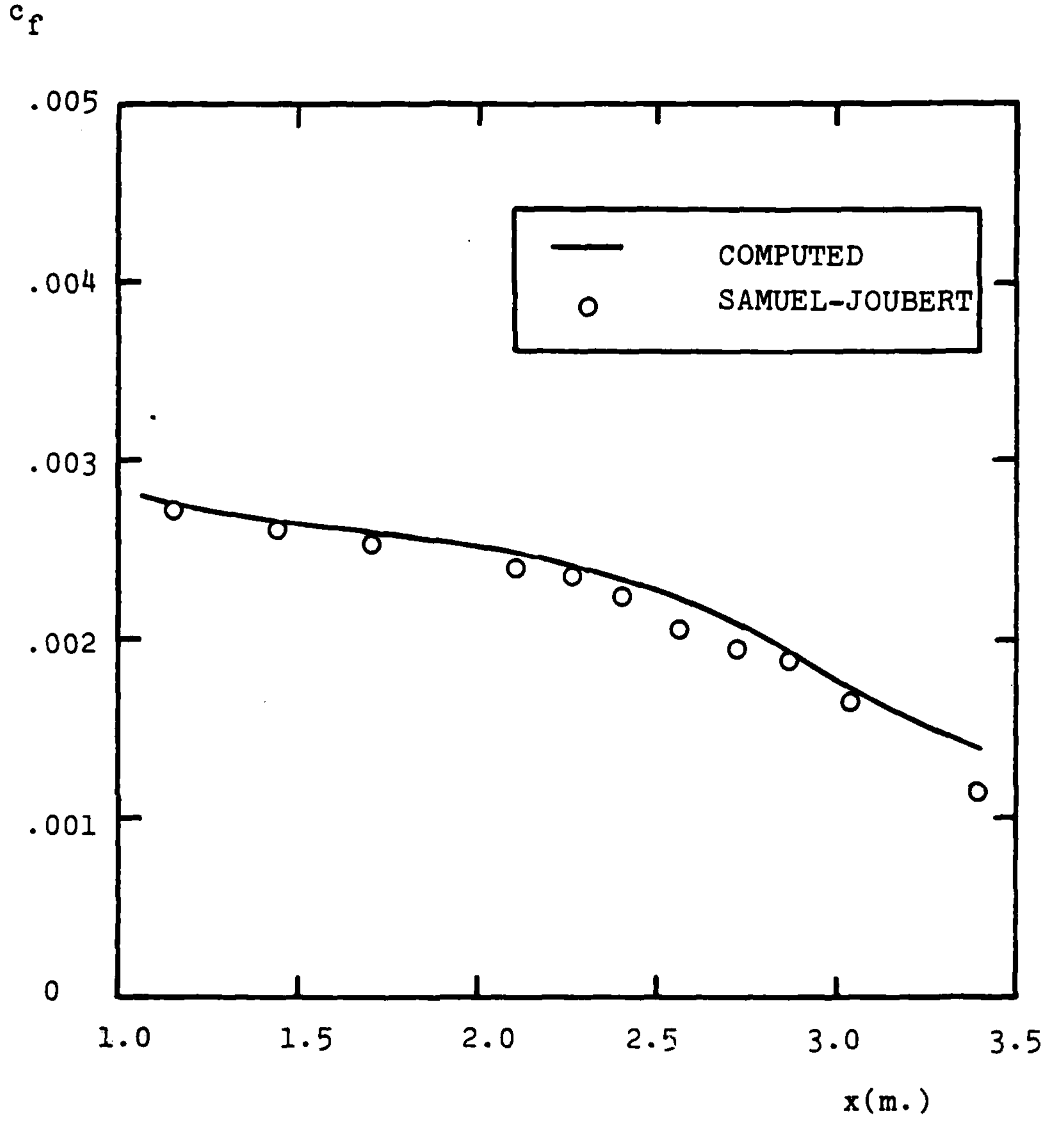

Figure 18. Comparison of computed and measured skin friction for the Samuel-Joubert adverse-pressure-gradient boundary layer.

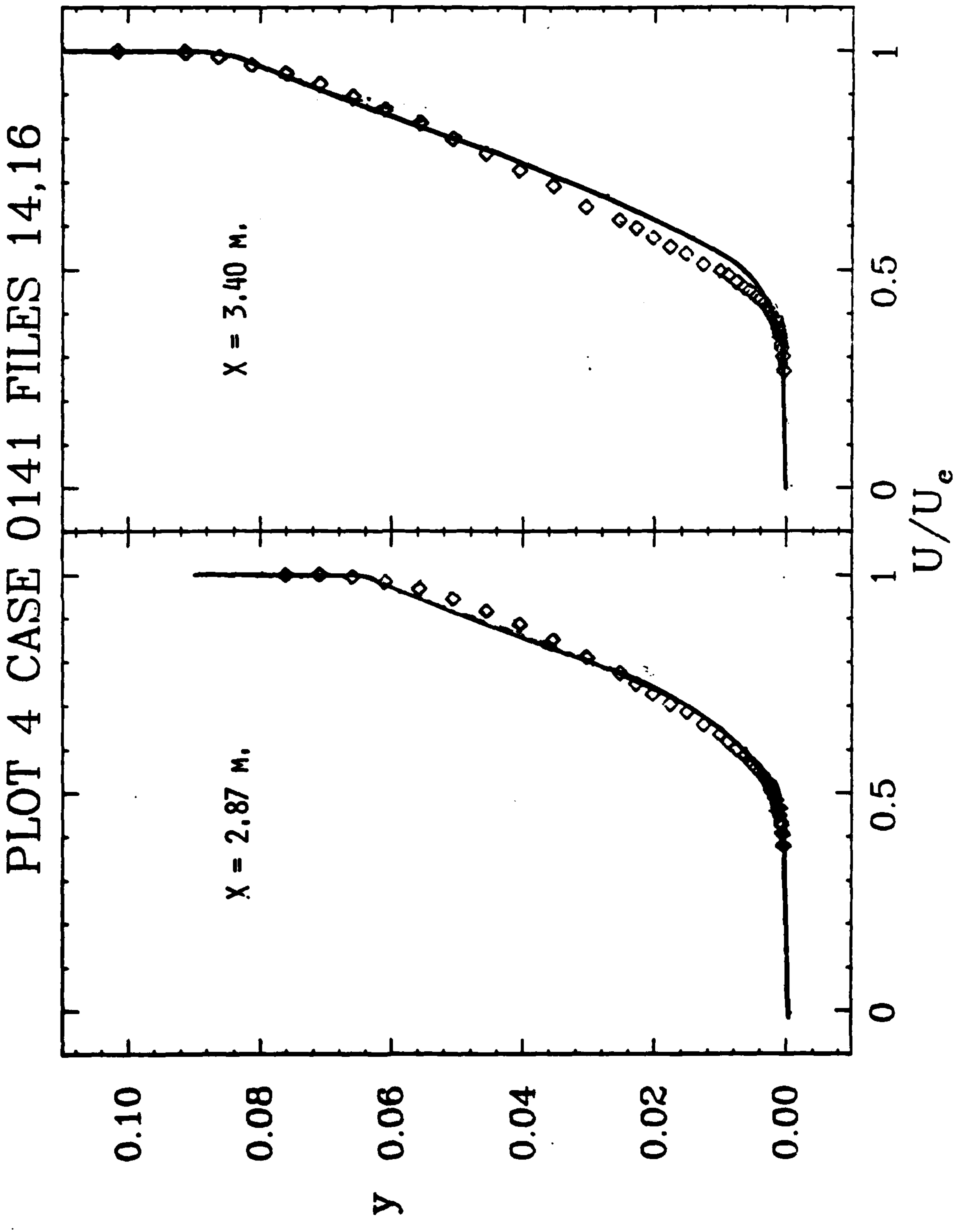

Figure 19. Incompressible boundary layer with adverse pressure gradient.

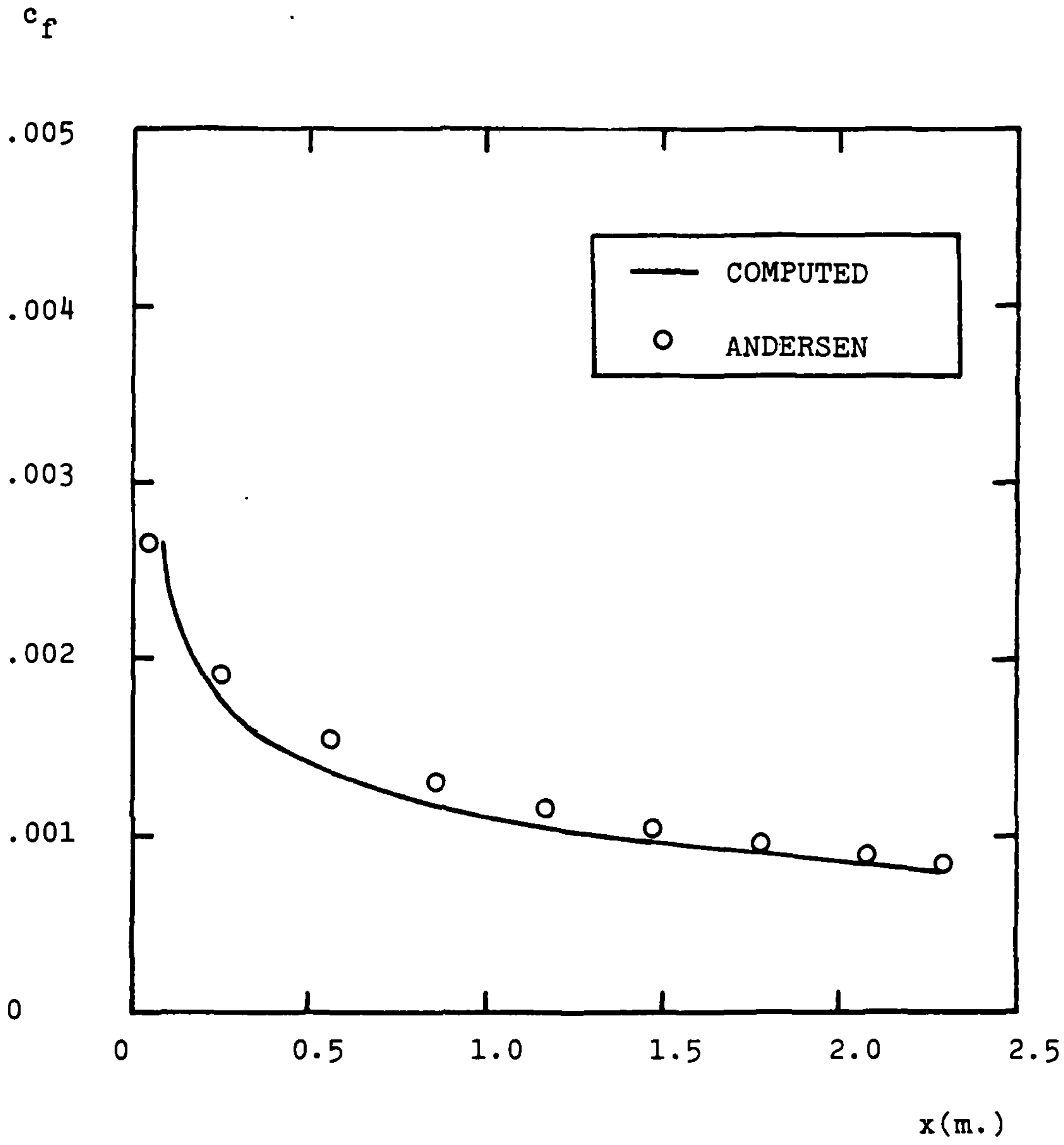

Figure 20. Comparison of computed and measured skin friction for a boundary layer with constant pressure and uniform mass injection; $v_w = .00375\ U_e$.

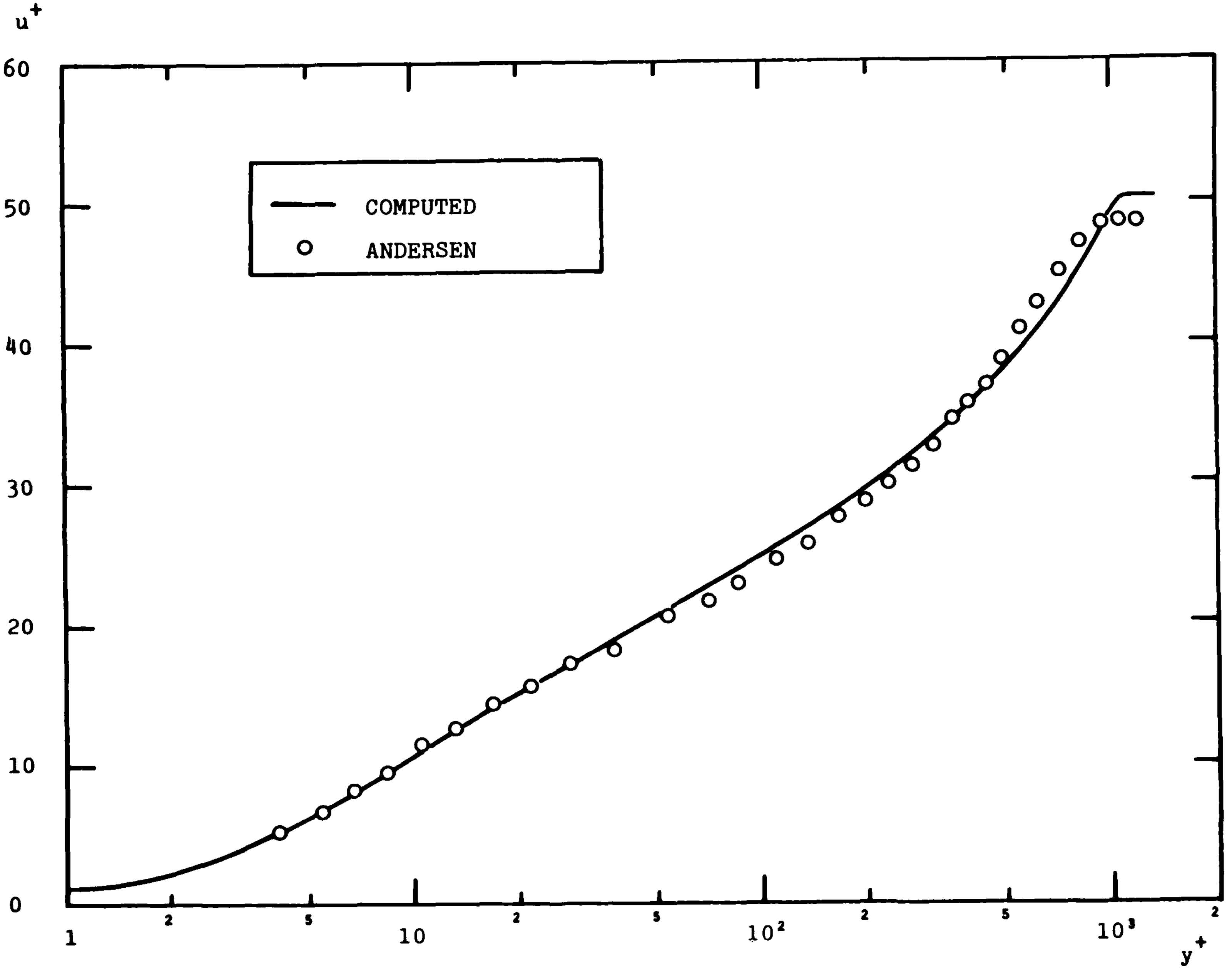

Figure 21. Comparison of computed and measured velocity profiles for a boundary layer with constant pressure and uniform mass injection; $v_w = .00375\ U_e$.

of scale while computed and measured velocity profiles are within 3 percent of each other.

Figures 22 and 23 compare computed and measured skin friction and velocity profiles, respectively, for the suction case. As shown, after the initial transient (caused by a poor choice of initial k and profiles), computed skin friction asymptotes to a value 4 percent higher than measured. The computed velocity profile lies within 5 percent of corresponding measurements.

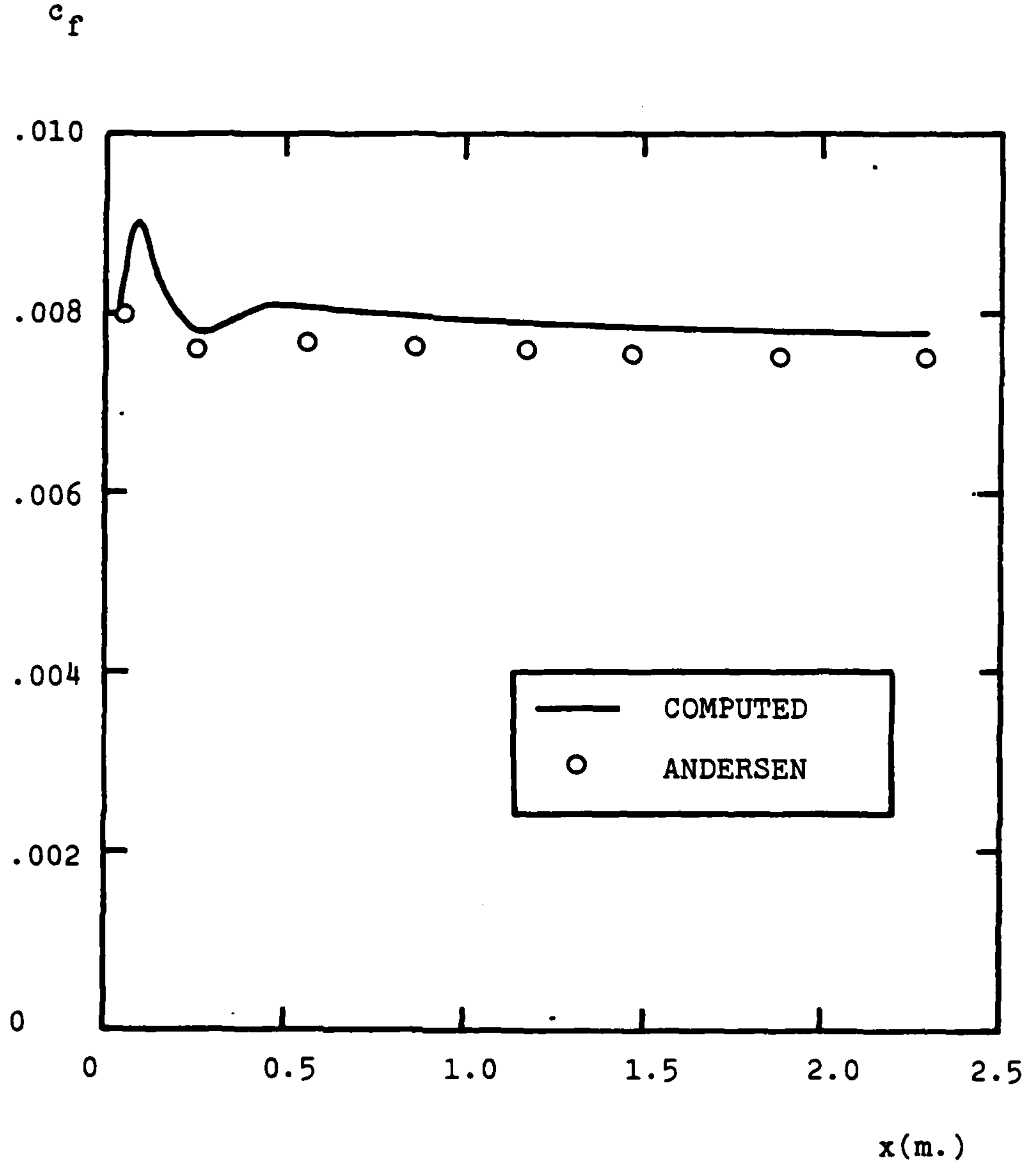

Figure 22. Comparison of computed and measured skin friction for a boundary layer with mild adverse pressure gradient and uniform suction; $v_w = -.00375\ U_e$.

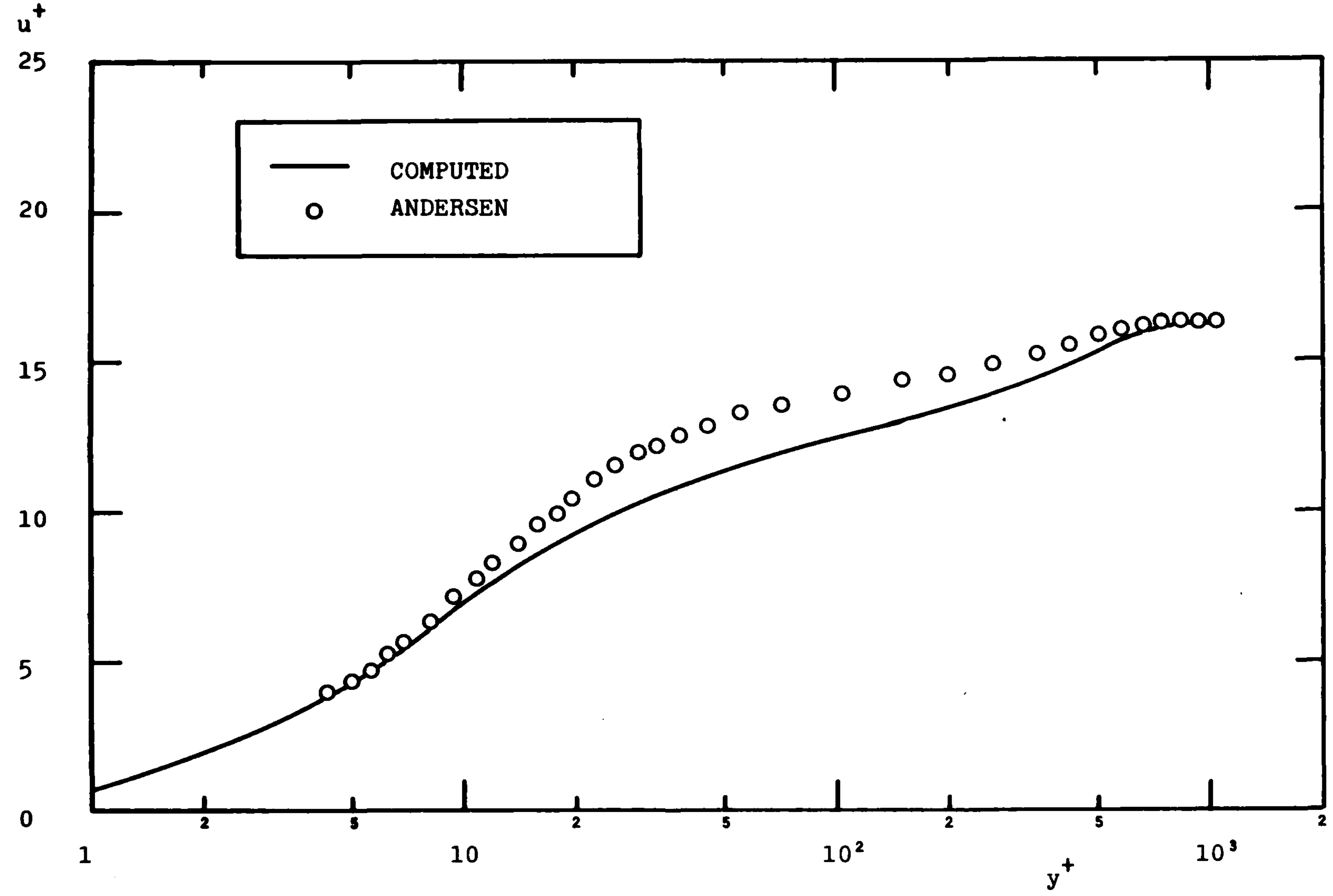

Figure 23. Comparison of computed and measured velocity profiles for a boundary layer with mild adverse pressure gradient and uniform suction; $v_w = -.00375\ U_e$.

6. SUMMARY AND CONCLUSIONS

The primary objectives of this study have been accomplished, viz, we have made a critical review of closure approximations used in two-equation turbulence models and determined what appears to be an optimum choice of dependent variables. As a result, we have developed a new two-equation model which shows promise of being more accurate for boundary layers in an adverse pressure gradient than any other similar model.

As in our prior turbulence modeling efforts, we have made extensive use of perturbation methods (Sections 3 and 4). In contrast to prior studies, our analysis of the defect layer includes pressure gradient. As discussed in Section 3, limiting the defect-layer analysis to the constant-pressure case displays little difference amongst the various two-equation models in general usage. However, as soon as an adverse pressure gradient is included, the models exhibit large differences. As a general observation, the Second Stanford Olympiad demonstrated that modern turbulence models are not much more accurate than those in use 15 years ago if the flow of concern is a boundary layer in adverse pressure gradient. The analysis of Section 3 indicates why this is true and, with the introduction of the new model, offers the basis for development of new models which are accurate for such flows.

The model thus far has been tested for five incompressible boundary layers. Certainly much more testing is needed before the model can be offered for general use. Additional testing will be done in future research efforts. However, additional development of the model will be needed before such tests can or should be done. Specifically, the model must be generalized for compressibility and, even more importantly, the constitutive relation between Reynolds stress and mean-flow properties must be revised. The relation proposed in Equation (6) fails to predict anisotropy of the normal stresses, and does not account for streamline curvature effects. Additionally, it is not at all clear that model predictions will bear any relation to physical reality for flows which are unsteady. Because unsteady boundary layers are of key interest in the overall Contract objectives, future development efforts must include unsteady flow analysis and application.

APPENDIX A: DEFECT-LAYER EQUATIONS

In this Appendix, we present details of the formal perturbation expansion solution to the defect-layer equations. First, we summarize the three turbulence models under consideration. Next, we outline the form of the perturbation expansions and state the equations for the leading order terms in the expansions. Then, we present boundary conditions used in solving the defect-layer equations. Finally, we indicate the manner in which skin friction and wake strength can be extracted from the defect-layer solution.

A.1 TURBULENCE MODELS UNDER CONSIDERATION

In analyzing the defect layer, we focus on three turbulence models, viz, the new model postulated in Section 2, the Wilcox-Rubesin model (Ref 9) and the Jones-Launder model (Ref 5). For all three of the models we must solve the equations for mean mass and momentum conservation, an equation for a turbulent energy scale and an equation for a turbulent dissipation scale. For all three models, the first three equations assume the following form.

$$\frac{\partial u}{\partial x} + \frac{\partial v}{\partial y} = 0 \qquad (A.1)$$

$$u\frac{\partial u}{\partial x} + v\frac{\partial u}{\partial y} = U_e\frac{dU_e}{dx} + \frac{\partial}{\partial y}\left\{\nu_T\frac{\partial u}{\partial y}\right\} \qquad (A.2)$$

$$u\frac{\partial k}{\partial x} + v\frac{\partial k}{\partial y} = \nu_T\left[\frac{\partial u}{\partial y}\right]^2 - \epsilon + \frac{\partial}{\partial y}\left\{\sigma^*\nu_T\frac{\partial k}{\partial y}\right\} \qquad (A.3)$$

Note that Equations (A.1-A.3) do not include molecular viscosity. This is a valid approximation in the defect layer as the eddy viscosity is proportional to $U_e\delta^*$, where U_e is the boundary-layer-edge velocity and δ^* is displacement thickness. Hence, the ratio of molecular to eddy viscosity varies inversely with displacement-thickness Reynolds number and is thus very small. The difference amongst the three models is the way the dissipation, ϵ , and the eddy viscosity, ν_T, are computed.

A.1.1 New Model

For this model, in addition to Equations (A.1-A.3) we have:

$$\epsilon = \beta^*\omega k \qquad (A.4a)$$

$$\nu_T = k/\omega \qquad (A.5a)$$

$$u\frac{\partial \omega}{\partial x} + v\frac{\partial \omega}{\partial y} = \gamma\left[\frac{\partial u}{\partial y}\right]^2 - \beta\omega^2 + \frac{\partial}{\partial y}\left\{\sigma\nu_T\frac{\partial \omega}{\partial y}\right\} \qquad (A.6a)$$

Leaving σ and σ^* undetermined, the values for the remaining closure coefficients are:

$$\left.\begin{array}{l} \beta = 3/40 \quad , \quad \beta^* = 9/100 \\ \gamma = \frac{5}{6} - \frac{5}{9}\sigma \end{array}\right\} \qquad \text{(A.7a)}$$

A.1.2 Wilcox-Rubesin Model

In this model, the additional equations are as follows.

$$\varepsilon = \beta^* \omega k \qquad \text{(A.4b)}$$

$$\nu_T = k/\omega \qquad \text{(A.5b)}$$

$$u\frac{\partial \omega^2}{\partial x} + v\frac{\partial \omega^2}{\partial y} = \gamma\omega\left[\frac{\partial u}{\partial y}\right]^2 - \left\{\beta + \sigma_d\left[\frac{\partial \ell}{\partial y}\right]^2\right\}\omega^3 + \frac{\partial}{\partial y}\left\{\sigma\nu_T\frac{\partial \omega^2}{\partial y}\right\} \qquad \text{(A.6b)}$$

where $\ell = \sqrt{k}/\omega$. Values for the closure coefficients are:

$$\left.\begin{array}{lll} \beta = 3/20 & , & \beta^* = 9/100 \\ \sigma = 1/2 & , & \sigma^* = 1/2 \\ \sigma_d = 1 & , & \gamma = 10/9 \end{array}\right\} \qquad \text{(A.7b)}$$

A.1.3 Jones-Launder Model

In this model we compute dissipation, ε , directly and so that the additional equations are:

$$\nu_T = \beta^* k^2 / \varepsilon \qquad \text{(A.5c)}$$

$$u\frac{\partial \varepsilon}{\partial x} + v\frac{\partial \varepsilon}{\partial y} = \beta^* c_1 k\left[\frac{\partial u}{\partial y}\right]^2 - c_2\varepsilon^2/k + \frac{\partial}{\partial y}\left\{\sigma\nu_T\frac{\partial \varepsilon}{\partial y}\right\} \qquad \text{(A.6c)}$$

Values for the closure coefficients are:

$$\left.\begin{array}{lll} & \beta^* = 9/100 & \\ c_1 = 31/20 & , & c_2 = 2 \\ \sigma^* = 1 & , & \sigma = 10/13 \end{array}\right\} \qquad \text{(A.7c)}$$

A.2 EXPANSION PROCEDURE

Following the formulation of Wilcox and Traci (Ref 8), we introduce a streamfunction ψ, and seek a perturbation solution of the form:

$$\psi = U_e \Delta \left\{ \eta - \frac{u_\tau}{U_e} F_1 + \ldots \right\} \tag{A.8}$$

$$k = \frac{u_\tau^2}{\sqrt{\beta^*}} \left\{ K_o + \ldots \right\} \tag{A.9}$$

$$\omega = \frac{u_\tau}{\sqrt{\beta^*}\Delta} \left\{ W_o + \ldots \right\} \tag{A.10}$$

$$\varepsilon = \frac{u_\tau^3}{\Delta} \left\{ E_o + \ldots \right\} \tag{A.11}$$

where

$$\eta = y/\Delta \quad , \quad \Delta = U_e \delta^* / u_\tau \tag{A.12}$$

Inserting Equations (A.8–A.12) into Equations (A.1–A.7), neglecting higher-order terms, letting N_o denote dimensionless eddy viscosity, and defining

$$U_1 = \partial F_1 / \partial \eta \quad , \quad L_o = \sqrt{K_o} / W_o \tag{A.13}$$

we obtain the following equations.

$$\frac{\partial}{\partial \eta}\left\{ N_o \frac{\partial U_1}{\partial \eta} \right\} + (\alpha_T - 2\beta_T - 2\omega_T)\eta \frac{\partial U_1}{\partial \eta} + (\beta_T - 2\omega_T) U_1 = 2\sigma_T x \frac{\partial U_1}{\partial x} \tag{A.14}$$

$$\sigma^* \frac{\partial}{\partial \eta}\left\{ N_o \frac{\partial K_o}{\partial \eta} \right\} + (\alpha_T - 2\beta_T - 2\omega_T)\eta \frac{\partial K_o}{\partial \eta} - 4\omega_T K_o + \sqrt{\beta^*}\left\{ N_o \left[\frac{\partial U_1}{\partial \eta}\right]^2 - E_o \right\} = 2\sigma_T x \frac{\partial K_o}{\partial x} \tag{A.15}$$

where

$$E_o = K_o W_o \tag{A.16}$$

and

$$N_o = K_o / W_o = K_o^2 / E_o \tag{A.17}$$

The final equation for each model is different; the equations are:

New Model

$$\sigma\frac{\partial}{\partial\eta}\left\{N_o\frac{\partial W_o}{\partial\eta}\right\} + (\alpha_T-2\beta_T-2\omega_T)\,\eta\frac{\partial W_o}{\partial\eta} + (\alpha_T-\beta_T-4\omega_T)W_o$$
$$\sqrt{\beta^*}\left\{\gamma\left[\frac{\partial U_1}{\partial\eta}\right]^2 - \frac{\beta}{\beta^*}W_o^2\right\} = 2\sigma_T x\,\frac{\partial W_o}{\partial x} \qquad \text{(A.18a)}$$

Wilcox-Rubesin Model

$$\sigma\frac{\partial}{\partial\eta}\left\{N_o\frac{\partial W_o^2}{\partial\eta}\right\} + (\alpha_T-2\beta_T-2\omega_T)\,\eta\frac{\partial W_o^2}{\partial\eta} + (\alpha_T-\beta_T-4\omega_T)W_o^2$$
$$- \sigma_d\left[\frac{\partial L_o}{\partial\eta}\right]^2 W_o^3 + \sqrt{\beta^*}\left\{\gamma W_o\left[\frac{\partial U_1}{\partial\eta}\right]^2 - \frac{\beta}{\beta^*}W_o^3\right\} = 2\sigma_T x\,\frac{\partial W_o^2}{\partial x} \qquad \text{(A.18b)}$$

Jones-Launder Model

$$\sigma\frac{\partial}{\partial\eta}\left\{N_o\frac{\partial E_o}{\partial\eta}\right\} + (\alpha_T-2\beta_T-2\omega_T)\,\eta\frac{\partial E_o}{\partial\eta} + (\alpha_T-\beta_T-8\omega_T)E_o$$
$$\sqrt{\beta^*}\left\{\frac{c_1}{\beta}K_o\left[\frac{\partial U_1}{\partial\eta}\right]^2 - c_2E_o^2/K_o\right\} = 2\sigma_T x\,\frac{\partial E_o}{\partial x} \qquad \text{(A.18c)}$$

where the parameters α_T, β_T, σ_T and ω_T are defined in terms of δ^*, u_τ and skin friction, $c_f = 2u_\tau^2/U_e^2$, i.e.,

$$\left.\begin{aligned}
\alpha_T &= (2/c_f)d\delta^*/dx \\
\beta_T &= (\delta^*/\tau_w)dp/dx \\
\sigma_T &= \delta^*/(c_f x) \\
\omega_T &= (\delta^*/c_f u_\tau)du_\tau/dx
\end{aligned}\right\} \qquad \text{(A.19)}$$

Equations (A.14-A.18) will have self-similar solutions only if α_T, β_T and ω_T are independent of x. As noted by Bush and Fendell (Ref 14), for $Re_{\delta*} >> 1$, u_τ varies sufficiently slowly that we have

$$\omega_T = o(1) \qquad \text{as} \qquad Re_{\delta*} \to \infty \qquad \text{(A.20)}$$

and, in addition, the shape factor to leading order approaches one which (from inspection of the momentum-integral equation) implies

$$\alpha_T \to 1 + 3\beta_T \qquad \text{as} \qquad Re_{\delta*} \to \infty \qquad \text{(A.21)}$$

Thus, self-similar solutions exist provided the parameter β_T is independent of x.

In summary, the defect-layer equations for the leading order terms in the perturbation expansions become:

All Models

$$\frac{d}{d\eta}\left\{N_o\,\frac{dU_1}{d\eta}\right\} + (1+\beta_T)\eta\frac{dU_1}{d\eta} + \beta_T U_1 = 0 \qquad \text{(A.22)}$$

$$\sigma^*\frac{d}{d\eta}\left\{N_o\,\frac{dK_o}{d\eta}\right\} + (1+\beta_T)\eta\frac{dK_o}{d\eta} + \sqrt{\beta^*}\left\{N_o\left\{\frac{dU_1}{d\eta}\right\}^2 - E_o\right\} = 0 \qquad \text{(A.23)}$$

New Model

$$\sigma\,\frac{d}{d\eta}\left\{N_o\,\frac{dW_o}{d\eta}\right\} + (1+\beta_T)\eta\frac{dW_o}{d\eta} + (1+2\beta_T)W_o + \sqrt{\beta^*}\left\{\gamma\left\{\frac{dU_1}{d\eta}\right\}^2 - \frac{\beta}{\beta^*}\,W_o^2\right\} = 0 \qquad \text{(A.24a)}$$

Wilcox-Rubesin Model

$$\sigma\,\frac{d}{d\eta}\left\{N_o\,\frac{dW_o^2}{d\eta}\right\} + (1+\beta_T)\eta\frac{dW_o^2}{d\eta} + 2(1+2\beta_T)W_o^2 - \sigma_d\left\{\frac{dL_o}{d\eta}\right\}^2 W_o^3 + \sqrt{\beta^*}\left\{\gamma W_o\left\{\frac{dU_1}{d\eta}\right\}^2 - \frac{\beta}{\beta^*}\,W_o^3\right\} = 0 \qquad \text{(A.24b)}$$

Jones-Launder Model

$$\sigma\,\frac{d}{d\eta}\left\{N_o\,\frac{dE_o}{d\eta}\right\} + (1+\beta_T)\eta\frac{dE_o}{d\eta} + (1+2\beta_T)E_o + \sqrt{\beta^*}\left\{\frac{c_1}{\beta^*}K_o\left\{\frac{dU_1}{d\eta}\right\}^2 - c_2\,\frac{E_o^2}{K_o}\right\} = 0 \qquad \text{(A.24c)}$$

A.3 BOUNDARY CONDITIONS

At the outer edge of the defect layer, we pose the conditions that the velocity equal the freestream velocity. Additionally, we let the turbulent energy assume a small value and insist that the turbulent length scale have zero slope at the boundary-layer edge. In their defect-layer analysis, Wilcox and Traci used these boundary conditions as well as explicitly prescribing both K_o and W_o. Thus,

$$\left.\begin{aligned} U_1 &= 0 \\ K_o &= \text{small value} \\ dL_o/d\eta &= 0 \end{aligned}\right\} \quad \text{at} \quad \eta = \eta_e \qquad \text{(A.25)}$$

Approaching the surface, we must formally match to the law of the wall. Matching is a bit different for each model but is nevertheless straightforward; details of the algebra will thus be omitted in the interest of brevity. The limiting forms we have used for $\eta \to 0$ follow.

$$\left.\begin{array}{l} U_1 \sim \frac{1}{\kappa}\left\{-\ln\eta + u_o - u_1\eta\ln\eta\right\} \\ K_o \sim \left\{1 + k_1\eta\ln\eta\right\} \\ W_o \sim \frac{1}{\kappa\eta}\left\{1 + w_1\eta\ln\eta\right\} \\ E_o \sim \frac{1}{\kappa\eta}\left\{1 + e_1\eta\ln\eta\right\} \end{array}\right\} \quad \text{as } \eta \to 0 \qquad \text{(A.26)}$$

The coefficients u_1, k_1, w_1 and e_1 are as follows.

$$k_1 = \frac{\beta_T/\kappa}{\left(\frac{\sigma^*\kappa^2}{2\sqrt{\beta^*}} - 1\right)} \qquad \text{(A.27)}$$

New Model

$$u_1 = \frac{\beta}{\gamma\beta^*}\,\frac{\sigma^*\kappa^2}{2\sqrt{\beta^*}}\,k_1/(1 - \beta/\gamma\beta^*) \qquad \text{(A.28a)}$$

$$w_1 = \frac{\sigma^*\kappa^2}{2\sqrt{\beta^*}}\,k_1/(1 - \beta/\gamma\beta^*) \qquad \text{(A.29a)}$$

Wilcox-Rubesin Model

$$u_1 = \frac{\frac{\sigma^*\kappa^2}{2\sqrt{\beta^*}}\left(\frac{\beta}{\beta^*}\sqrt{\beta^*} + (2\sigma-\sigma_d)\kappa^2\right) + (\sigma_d-\sigma)\kappa^2}{2\gamma\sqrt{\beta^*}(1-\beta/\gamma\beta^*) + 2\sigma\kappa^2}\,k_1 \qquad \text{(A.28b)}$$

$$w_1 = \frac{\frac{\sigma^*\kappa^2}{2\sqrt{\beta^*}}\,\gamma\sqrt{\beta^*} + (\sigma_d-\sigma)\kappa^2}{2\gamma\sqrt{\beta^*}(1-\beta/\gamma\beta^*) + 2\sigma\kappa^2}\,k_1 \qquad \text{(A.29b)}$$

Jones-Launder Model

$$u_1 = \frac{\left(1 + \sigma^*\kappa^2/\sqrt{\beta^*}\right)c_2/c_1 - 1}{2(1 - c_2/c_1)}\,k_1 \qquad \text{(A.28c)}$$

$$e_1 = \frac{\left(1 + \sigma^*\kappa^2/\sqrt{\beta^*}\right) - c_2/c_1}{2(1 - c_2/c_1)}\,k_1 \qquad \text{(A.29c)}$$

Additionally, the coefficient u_o is determined from the integral constraint for mass conservation, viz,

$$\int_0^{\eta_e} U_1(\eta)\,d\eta = 1 \qquad \text{(A.30)}$$

To implement Equation (A.30) in the numerical solution of the defect-layer equations, we proceed as follows. Because the velocity is singular at $\eta = 0$, we integrate the numerical velocity profile from a point above the surface which we denote by η_L (typically of order .001 to .01) to the edge of the boundary layer, η_e. Then, we integrate the asymptotic profile for $U_1(\eta)$ given in Equations (A.26) from $\eta = 0$ to $\eta = \eta_L$. The latter integration involves the unknown coefficient u_o. Finally, the sum of these two integrals must be unity by virtue of Equation (A.30).

A.4 SKIN FRICTION AND WAKE STRENGTH

It is possible to determine the skin friction implied by the solution to the defect-layer equations by formal matching to the sublayer asymptotic velocity profile. Considering only leading order terms, this means we say:

$$\lim_{y^+\to\infty}\left[\frac{1}{\kappa}\,\ell n y^+ + B\right] = \lim_{\eta\to 0}\left[U_e/u_\tau + \frac{1}{\kappa}\,\ell n\eta - u_o/\kappa\right] \qquad \text{(A.31)}$$

There follows immediately, noting that $y^+ = \eta/Re_{\delta*}$ and $u_\tau/U_e = \sqrt{c_f/2}$

$$\sqrt{\frac{2}{c_f}} = (B + u_o/\kappa) + \frac{1}{\kappa}\,\ell n Re_{\delta*} \qquad \text{(A.32)}$$

Finally, combining Coles' composite profile [Equation (19)] with Equation (A.32) and evaluating the resulting equation at the boundary-layer edge, we arrive at the following expression for wake strength, $\tilde{\pi}$:

$$\tilde{\pi} = \frac{1}{2}\left(u_o - \ell n\eta_e\right) \qquad \text{(A.33)}$$

APPENDIX B: VISCOUS MODIFICATIONS

As noted in Section 4, very close to the surface the new model equations predict the turbulent energy tends to zero as distance to the 3.23 power. By contrast, if the quantity k is turbulent kinetic energy we would expect to have $k \sim y^2$ as $y \to 0$. Alternatively, if k is kinetic energy of surface-normal fluctuations, we would expect to have $k \sim y^4$ as $y \to 0$. Either way, we do not expect to have a non-integer exponent such as 3.23.

While, on the one hand, this feature of model predictions is of minor interest, there are other shortcomings of the model as formulated in Sections 2-4 which are not necessarily minor. For example, if transition from laminar to turbulent flow is important for a given application, the model must be altered in order to achieve physically realistic predictions. Additionally, predictions for low-Reynolds-number turbulent flows conceivably are inaccurate if no provision is made for viscous effects upon the various closure coefficients. To make provision for extending the model's applicability to such flows, this Appendix summarizes the required viscous modifications to the model equations.

For two-dimensional boundary layers, the model equations assume the following form:

$$u\frac{\partial k}{\partial x} + v\frac{\partial k}{\partial y} = \nu_T\left(\frac{\partial u}{\partial y}\right)^2 - \beta^*\omega k + \frac{\partial}{\partial y}\left[(\nu+\sigma^*\nu_T)\frac{\partial k}{\partial y}\right] \tag{B.1}$$

$$u\frac{\partial \omega}{\partial x} + v\frac{\partial \omega}{\partial y} = \gamma\left(\frac{\partial u}{\partial y}\right)^2 - \beta\omega^2 + \frac{\partial}{\partial y}\left[(\nu+\sigma\nu_T)\frac{\partial \omega}{\partial y}\right] \tag{B.2}$$

where

$$\nu_T = \gamma^* k/\omega \tag{B.3}$$

and the closure coefficients are:

$$\begin{aligned} \beta &= 3/40, \quad \sigma = 1/2, \quad \sigma^* = 1/2 \\ \beta^* &= \frac{9}{100}\left[1 + \frac{2}{3}\exp(-Re_T/4)\right] \\ \gamma^* &= 1 - (1-\lambda^2)\exp(-Re_T/R_k) \\ \gamma &= \frac{5}{9}\left[1 - (1-\lambda^2)\exp(-Re_T/R_\omega)\right] \end{aligned} \tag{B.4}$$

Additionally, the quantities Re_T , λ , R_k and R_ω are given by

$$Re_T = k/\omega\nu \quad ; \quad \lambda = \sqrt{6}/55 \quad ; \quad R_k = 1 \quad ; \quad R_\omega = 9/4 \qquad (B.5)$$

The rationale for the modified closure coefficients follows.

Considering first the coefficient β^* , the model-predicted very near wall behavior of k now becomes $k \sim y^4$ as $y \to 0$. Thus, our prediction indicates k is most appropriately identified as being the kinetic energy of the fluctuations normal to the surface. In addition, the coefficient 4 in the exponential damping term has been chosen to yield satisfactory agreement with the experimental data of Batchelor and Townsend (Ref 23) for the late-time decay of homogeneous turbulence.

Turning now to the coefficients γ and γ^* , Wilcox and Rubesin (Ref 9) found similar modifications necessary in their model in order to achieve physically acceptable predictions in the viscous sublayer. The indicated choice of the coefficient λ guarentees that in a Blasius boundary layer, turbulent energy will only be amplified for Reynolds number exceeding the linear-stability minimum-critical Reynolds number. The values for R_k and R_ω have been determined by analyzing the smooth-surface viscous sublayer. The values quoted insure the model predicts the additive constant in the law of the wall is 5.0.

We have rerun the Section 5 boundary-layer test cases using Equations (B.1-B.5). In none of the cases have we detected significant differences from results obtained when no viscous modifications appear in the model equations. However, we do notice a 20% increase in computing time because of the many exponentials which must be evaluated at every mesh point. We thus conclude that the viscous modifications proposed in Equations (B.1-B.5) add little to the model for fully-turbulent boundary-layer applications.

REFERENCES

1. Cebeci, T. and Smith, A.M.O., Analysis of Turbulent Boundary Layers, Ser in Appl Math & Mech, Vol XV, Academic Press (1974).

2. Coles, D.E. and Hirst, E.A., "Computation of Turbulent Boundary Layers - 1968 AFOSR-IFP-Stanford Conference," Vol II, Stanford Univ (1969).

3. Bradshaw, P., Ferriss, D.H. and Atwell, N.P., "Calculation of Boundary Layer Development Using the Turbulent Energy Equation," JFM, Vol 28, Pt 3, pp 593-616 (1967).

4. Donaldson, C.duP., "Calculation of Turbulent Shear Flows for Atmospheric and Vortex Motions," AIAA J, Vol 10, No 1, pp 4-12 (1972).

5. Jones, W.P. & Launder, B.E., "The Prediction of Laminarization with a Two-Equation Model of Turbulence," Int J Heat and Mass Trans, Vol 15, pp 301-314 (1972).

6. Wilcox, D.C. and Alber, I.E., "A Turbulence Model for High Speed Flows," Proc of the 1972 Heat Trans & Fluid Mech Inst, Stanford Univ Press, pp 231-252 (1972).

7. Saffman, P.G. and Wilcox, D.C., "Turbulence-Model Predictions for Turbulent Boundary Layers," AIAA J, Vol 12, No 4, pp 541-546 (1974).

8. Wilcox, D.C. and Traci, R.M., "A Complete Model of Turbulence," AIAA Paper 76-351 (1976).

9. Wilcox, D.C. and Rubesin, M.W., "Progress in Turbulence Modeling for Complex Flow Fields Including Effects of Compressibility," NASA TP 1517 (1980).

10. Kline, S.J., Cantwell, B.J. & Lilley, G.M., "1980-81 AFOSR-HTTM-Stanford Conference on Complex Turbulent Flows," Stanford Univ (1981).

11. MacCormack, R.W., "A Numerical Method for Solving the Equations of Compressible Viscous Flow," AIAA Paper 81-0110 (1981).

12. Kolmogorov, A.N., "Equations of Turbulent Motion of an Incompressible Fluid," Izvestia Academy of Sciences, USSR; Physics, Vol 6, Nos 1 and 2, pp 56-58 (1942).

13. Townsend, A.A., The Structure of Turbulent Shear Flow, pp 107-108, Cambridge Univ Press, Cambridge/Second Edition (1976).

14. Bush, W.B. and Fendell, F.E., "Asymptotic Analysis of Turbulent Channel and Boundary-Layer Flow," JFM, Vol 56, Pt 4, pp 657-681 (1972).

15. Chambers, T.L. and Wilcox, D.C., "Critical Examination of Two-Equation Turbulence Closure Models for Boundary Layers," AIAA J, Vol 15, No 6, pp 821-828 (Jun 1977).

16. Laufer, J., "The Structure of Turbulence in Fully Developed Pipe Flow," NACA 1174 (1952).

17. Andersen, P.S., Kays, W.M. & Moffat, R.J., "The Turbulent Boundary Layer on a Porous Plate: An Experimental Study of the Fluid Mechanics for Adverse Free-Stream Pressure Gradients," Report No HMT-15, Dept Mech Eng, Stanford Univ, CA (1972).

18. Saffman, P.G., "A Model for Inhomogeneous Turbulent Flow," Proc Roy Soc, Lond, Vol A317, pp 417-433 (1970).

19. Schlichting, H., Boundary Layer Theory, Fourth Ed, McGraw-Hill, New York, pp 519-527 (1960).

20. Wilcox, D.C. and Chambers, T.L., "Further Refinement of the Turbulence-Model Transition-Prediction Technique," DCW Industries Report DCW-R-03-02 (1975).

21. Wilcox, D.C., "User's Guide for the EDDYBL Computer Program," DCW Industries Report No DCW-R-14-02 (1976).

22. Wilcox, D.C., "Boundary-Layer Development on Ship Hulls," DCW Industries Report No DCW-R-26-01 (1983).

23. Townsend, A.A., The Structure of Turbulent Shear Flow, pp 55-56, Cambridge Univ Press, Cambridge/Second Edition (1976).

DAT

FILM